UNIVERSIDAD NACIONAL AUTÓNOMA DE MÉXICO

PROGRAMA DE POSGRADO EN ASTROFÍSICA

Instituto de Radioastronomía y Astrofísica

CHARACTERIZING THE DUST CONTENT ON PROTOPLANETARY DISKS: THE CASE OF TW HYA AND HD 163296

PARA OPTAR POR EL GRADO DE
MAESTRO EN CIENCIAS (ASTROFÍSICA)

PRESENTA
OSMAR MANUEL GUERRA ALVARADO

TUTORES O TUTOR
DR. CARLOS CARRASCO-GONZÁLEZ, INSTITUTO DE RADIOASTRONOMÍA y ASTROFÍSICA

Cd. Mx. FEBRERO 2021

Contents

Abstract

In order to understand the origin of planetary systems we need first to understand how dust evolves in protoplanetary disks. Recently, the development of ALMA has allowed to observe the dust content of disks with unprecedented detail. It has been well established that most protoplanetary disks show substructures which are most probably related with high and low density dust regions. The exact origin of the substructures is still unclear, but there is a consensus about dust growth having a fundamental role on the origin of the observed substructures and the formation of planets. However, the study of their physical properties has resulted very difficult even with ALMA.
In this work we analyzed multi-wavelength high resolution observations of two protoplanetary disks (TW Hya and HD 163296). For these, we have observations at four wavelengths in the ranges from 0.9 millimeters to 3 millimeters. This allowed us to study the spectral energy distribution at each radius and estimate important physical properties for the dust: temperature, density and maximum particle size. The high angular resolution of this study allowed us to find not only the global properties, but also to distinguish differences between bright and dark rings present in these disks. Our results are compared with those previously obtained in HL Tau, a much younger disk (1 Myr), since these three are the only disks with a detailed study of the radial dust distribution. We discuss possible implications of our results in the dust evolution that will lead to the formation of planetary systems.

Keywords— protoplanetary disk, planet formation

Chapter 1

Introduction

1.1 Birth of planetary systems

Circumstellar disks form during the gravitational collapse of a star due to the conservation of angular momentum. At first these disks are accreting material rapidly onto the star (e.g. 10^{-6}, 10^{-7} $M_{\odot}yr^{-1}$) but eventually this accretion rate decreases and some small amount of material endures (Williams & Cieza 2011). The material of the disk is conformed by 99% gas and 1% dust and the total mass ranges from 0.001 to 0.3 solar masses with typical sizes of several dozens to 1000 astronomical units (e.g. Tsukagoshi et al. 2019). It is believed that circumstellar disks are protoplanetary, meaning that the dust and gas content in the disk will evolve to form planetary systems. This process requires that dust particles in the disk grow several orders of magnitude in size to form planetesimals (e.g. Testi et al. 2014). Protoplanetary disks dissipate in about 2-3 million years mainly due to some material forming planets and photoevaporation by stellar radiation coming from the central star (Ribas et al. 2014). Therefore, the process of planet formation through grain growth is expected to be relatively fast before the disk disappears.
To understand how planet formation takes place in a protoplanetary disk, we need to take into account dust evolution. The first step in this evolution depends on the growth of micron-sized dust grains to cm-sized pebbles and then into larger km-sized planetesimals, leading to the formation of planets (e.g. Testi et al. 2014, Johansen & Lambrechts 2017). Then, it is crucial to understand how, when and where does this growth starts. This process is expected to happen in the high density regions from the mid-plane of the protoplanetary disks where dust can collide, grow and migrate during the early lifetime of the disks(Brauer et al. 2008). Therefore, in order to study the dust properties of the dust emission, we need sensitive continuum observations at (sub)millimeter wavelengths, which allows to trace emission from the mid-plane.

1.2 ALMA's Revolution

Since 2014, high-resolution ALMA observations have led to a revolution in the study of protoplanetary disks. Now we are able to image the dust emission in great detail due to the extraordinary high resolution and sensitivity observations (e.g.,ALMA Partnership et al. 2015 ;Andrews et al. 2016 ; Isella et al. 2016; Keppler et al. 2018; Sallum et al. 2015). The most important result from high angular resolution observations is that dust distribution in protoplanetary disk is not smooth, but the dust is usually segregated in dense substructures. The most common substructures are concentric dark and bright rings (Dong et al. 2018,Andrews et al. 2018a, See Figure 1.1), which seem to be associated with annular regions of higher (i.e., rings)

and lower (i.e., gaps) density (Carrasco-González et al. 2019). Less commonly found, some disks also show spiral arms (e.g Pérez et al. 2016).

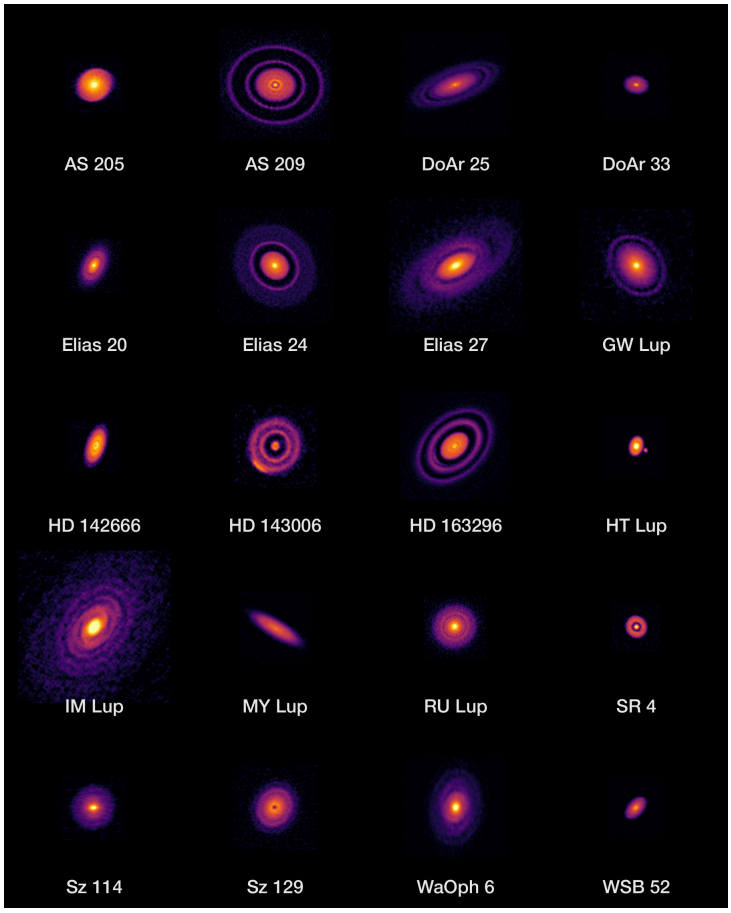

Figure 1.1: Images at 240 GHz of the continuum emission of the disks observed in the DSHARP survey (Andrews et al. 2018a). This images show the most commonly found substructures in protoplanetary disks, bright and dark rings which are regions of higher and lower density, respectively.

The origin of these substructures is not yet fully understood; many scenarios have been proposed, with the most promising one being related to planet-disk interactions (e.g., Dong et al. 2018, Zhu et al. 2014; Bae, Zhu, & Hartmann 2017; Zhang et al. 2018). However, other formation mechanisms not implying the presence of already formed protoplanets have been proposed: magnetized disks (Flock et al. 2015), fast pebble growth near condensation fronts (Zhang et al. 2015), and sintering[1]-induced dust rings (Okuzumi et al. 2016, Okuzumi & Tazaki 2019). Regardless of what the formation mechanism of the rings is, in pressure maxima, dust can be naturally trapped in the dense rings (e.g., Flock et al. 2015; Ruge et al. 2016; Pinilla et al. 2017) since they can stop the radial drift allowing the dust to eventually grow to larger sizes and to start the formation of planetesimals (Whipple 1972; Barge & Sommeria 1995; Brauer et al. 2008). Therefore, it is thought that substructures are closely related to planet formation but it is not clear whether planets form these substructures. In order to understand the origin of substructures and the role that they play in the planet formation process, it is fundamental to characterize their dust content. This can be done by analyzing the frequency dependency of the

[1]Sintering is the process of fusing grains together at a temperature slightly below the sublimation point. Sintered aggregates are characterized by thick joints, called necks, that connect the constituent grains (Okuzumi et al. 2016).

dust emission (SED, the spectral energy distribution), allowing us to accurately estimate the dust density, temperature, and particle size distribution in disk substructures.

1.3 Dust particle distribution in disks

The combined effect of dust growth and migration of the dust grains should result in a distribution with the maximum grain size increasing towards the inner radii. The predicted high efficiency for the radial migration of solids requires that substructures play a fundamental role stopping the dust migration, reconciling the drift and the planetesimals formation timescales problems (Andrews, S. M. 2020). Substructures stop the migration allowing dust particles to endure larger timescales without falling to the central star. These traps are also ideal places for dust to grow and eventually form planetesimals through direct gravitational collapse or triggering the streaming instability, for which particles up to 1 millimeter are required (Andrews, S. M. 2020).

One of the most important parameter which can be estimated with observations is the dust particle size distribution (e.g., Rodmann et al. 2006; Isella et al. 2010; Guilloteau et al. 2011; Macías et al. 2019). A way to do this, is by measuring the frequency dependence of the dust opacity coming from the (sub)millimeter emission. This is usually done by assuming that dust opacity is dominated by absorption and that the emission is optically thin. If these assumptions are valid, in the Rayleigh-Jeans regime we can infer the dust properties from the spectral index of the emission (e.g., Beckwith et al. 1990; Pérez et al. 2015; Tazzari et al. 2016). However, in the last years it has become clear that (sub)millimeter dust emission in protoplanetary disks could have a significant contribution from scattering (Liu 2019; Zhu et al. 2019; Sierra et al. 2020), making it extremely difficult to obtain dust properties directly from the spectral index.

The most detailed study up to day of the dust properties in a protoplanetary disk was performed by Carrasco-González et al. (2019) in HL Tau. This is one of the youngest disks (≈ 1 Myr) known to contain multiple substructures. It is also the disk with the largest number of high resolution millimeter continuum observations. Carrasco-González et al. (2019) combined observations with ALMA and VLA at four wavelengths (0.9, 1.3, 2.1 and 9 mm; See Figure 1.2). The large number of images covering a wide range of wavelengths allowed them to obtain the dust properties without any strong assumption. For instance, in this study the dust opacity was considered a combination from scattering and absorption and the emission was not assumed to be optically thin. From these, they were able to obtain the dust particle properties with a physical resolution of only 7.5 au, which allowed them to study differences in the particle properties in different rings. The most important result from this study is that particles had grown up to 1 millimeter in the HL Tau disk. These authors also discussed the formation mechanism of the different radial features. The large gap at 70 au seems to be related to the presence of a protoplanet. In contrast, several of the most internal (< 50 au) substructures could be associated with the presence of snowlines (see Figure 1.3). This work demonstrated the necessity of multiple high quality observations in order to properly characterize the dust size distribution in protoplanetary disks.

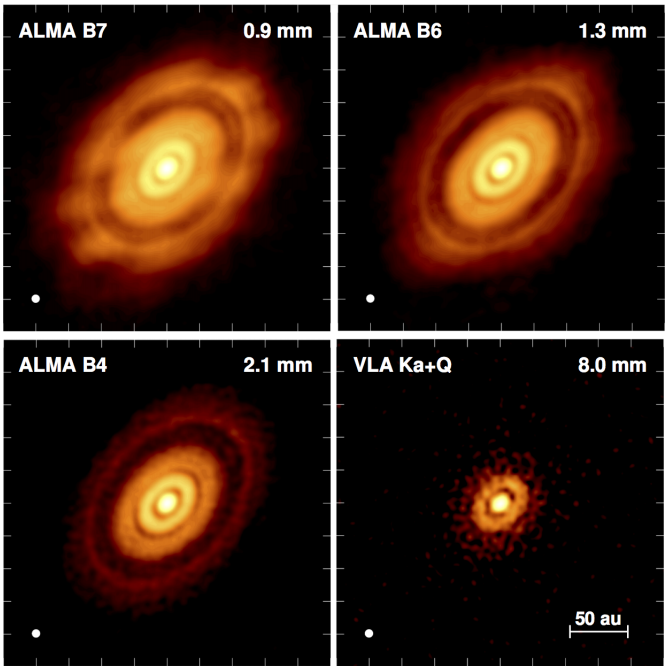

Figure 1.2: Final set of HL Tau images used in Carrasco-González et al. (2019). All images are convolved to the same angular resolution of 50 mas. Color scales in the four panels are between 2 times the rms of each map and the maximum intensity.

1.4 This work

In this work we present an analysis of high resolution ALMA observations of two protoplanetary disks, TW Hya and HD 163296. Both are relatively old disks (5-10 Myr) around solar and Herbig young stars respectively. Therefore, they represent a stage in the disk evolution much older than for HL Tau. TW Hya has a stellar mass of 0.6 $M_\odot$ and a luminosity of 0.23 $L_\odot$ (Sokal et al. 2018). HD 163296 has stellar mass of 1.9 $M_\odot$ (Setterholm et al. 2018) and a luminosity of 17 $L_\odot$ (Andrews et al. 2018a). For both of them we have high angular resolution ALMA observations at different bands covering a wide range of wavelengths (0.9, 1.2, 2.1 and 3 mm). We analyze the SED in this range at each radius in order to estimate the dust properties.

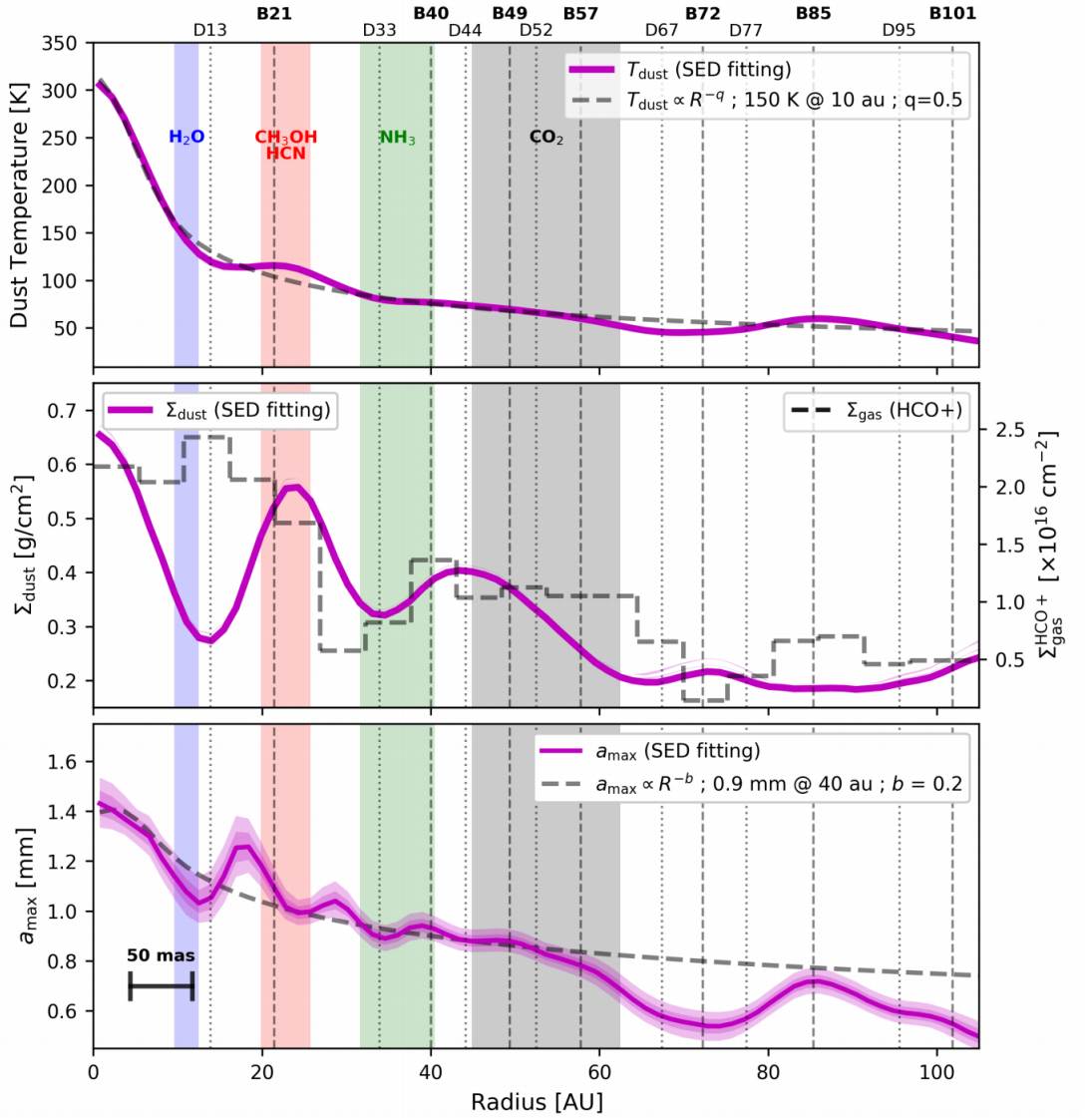

Figure 1.3: The dust distribution in HL Tau derived from the radial SED fitting of the ALMA and VLA data in Carrasco-González et al. (2019). *Top panel*: Dust Temperature radial profile. *Central panel*: Dust surface density. *Bottom panel*: Radial profile of the maximum dust particle size obtained from the SED fitting.

Chapter 2

Observations and data analysis

All the observations presented in this work were obtained with the Atacama Large Millimeter Array (ALMA). Most of the observations were obtained from the archive from previous observational projects with published results. We also present new observations of TW Hya at 3 millimeters which were obtained by our group. This work is the first time that these are analyzed all of them together. A summary of the observations used in this work can be found in Table 2.1 while the characteristics of the images used are shown in Table 2.2. In the following sections, we give a brief summary of basic interferometry and we show the observations and how we analyzed them.

2.1 Basic radio-interferometry

An interferometer consists of a number of antennas whose signals are combined in order to the whole array to operate as a single telescope with a size similar to the maximum separation between antennas. A baseline is defined as a pair of antennas, each baseline measures amplitude and phase in a single moment in time to a spatial scale inverse to the separation scale between antennas. Every pair of antennas in an instant of time measures a point in the uv plane, which is defined as the Fourier transform of the image plane. So, if we consider every pair of antennas in the whole interferometer, we have a coverage in the uv plane. In addition, by using the rotation of the Earth we can increase this coverage. The better the coverage of the uv plane is, the higher the quality of the final image will be. In the uv plane, the distance between antennas is given in units of the observed wavelength. Therefore, there are two possible ways to improve the coverage of the uv plane. One, is by observing longer observation times, while the other is observing in a wide range of frequencies. The largest observable scale if given by the inverse of the minimum baseline, therefore, for extended configurations we obtain high angular resolutions, but the sensitivity to large spatial scales decreases. Thus, it is important to include short baselines in the uv coverage to recover the flux for the large scales of the source.

An standard observation strategy consists on the observation of a phase calibrator together with the target. Since the light of a point source should arrive to all antennas at the same time (once geometrical delays are corrected), it is desirable to use a bright point source as the phase calibrator. It is also desirable for this source to be very close to our target in order to correct for phase delays due to the atmosphere. Fortunately, bright quasars are located everywhere in the sky and most of them are point sources. However, quasars are commonly variable and their flux density is usually unknown, therefore, we also need the observation of a flux calibrator in order to be able to transform the signal measurement by the antennas into a physical flux.

Once the data is calibrated in amplitude an phase, an image is done by applying the Fourier transform to the calibrated data. There are several ways to obtain an image from the calibrated data. The more often used is `clean`. There are several holes in the *uv* coverage which manifest as sidelobes in the PSF. `Clean` does a deconvolution and reconstructs the image replacing the dirty PSF by a cleaned one. In the imaging process of `clean` one can weight the visibilities of the data in differentes ways. Natural weighting assumes the same statistical weight for all the samples in the *uv* coverage. Since normally the inner *uv* plane has higher density of samples (higher SNR) than the outer *uv* plane, this will produce the lowest angular resolution but with great sensitivity to the larger scales. Uniform weighting divide the samples in cells giving them a value that is the average between the values of the samples of that specific cell. This weighting losses sensitivity to large spatial scale but has the maximum angular resolution possible. Briggs weighting varies between natural and uniform weighting, High SNR samples are uniform weighted to optimize for PSF shape, and low signal-to-noise data are naturally weighted to optimize for sensitivity.

2.1.1 TW Hya

We obtained new ALMA data at 3 millimeters for TW Hya during Cycle 6 in five different executions carried out from 2019 June 24 to 2019 July 08 (project code: 2018.1.01218.S). We also downloaded archival ALMA data at 0.9 mm, 1.2 mm and 2.1 mm. For all data, we followed the instructions from the reduction scripts to perform the calibration of the raw data using their corresponding version of `CASA` (Common Astronomy Software Applications). After checking and obtaining an acceptable calibration, we performed channel averaging (Resulting in 8 channel data sets) to each data set since we only needed the continuum emission. We also got lower resolution archival data at 3 mm, 2.1 mm, 1.2 mm and 0.9 mm to prevent from losing flux at the larger scales by covering shorter baselines. To be able to combine high and low resolution data we needed to correct for proper motions and astrometric errors between the different epochs. For this, we first centered each of these data sets by shifting their visibilities phase center using the `CASA` task `fixvis`. Then, we use the table tool in `CASA` to properly align the different data sets for each wavelength.

After the combination of the datasets, self-calibration was performed in order to improve the quality and correct for some of the small phase shifts produced by astrometric errors. Self-calibration was performed in two steps. First, we corrected only the phase in an iterative process, starting with longer time solution intervals and decreasing them until no improvement was seen in the peak signal-to-noise ratio (SNR) or until reaching the integration time of the data. The last step was the amplitude self-calibration, but it only provided improvement of the SNR in a few cases with low resolution and very high SNR, for this reason this was only applied in the low resolution data sets of each band. The final combined measurement sets were obtained after checking the data and self-calibration on each step and after recomputing the weights by using the `CASA` task `statwt`. Final images were done by using the task `tclean` with the multi-scale, multi-frequency synthesis algorithm (MS-MFS; Rau & Cornwell 2011). Since at each band we combined data at several frequencies (see Table 2.1) we used nterms = 2 in `tclean`, in order to correct for possible changes of the flux density with frequency. We used a pixel size of 0.1 times the major axis of the synthesized beam and scales of 0, 1, 3, 5 times the major axis of the synthesized beam of the image. After exploring different weighting values, we decided to go for a Briggs visibility weighting with different robust parameters for each image. Finally, to analyze these images together we needed to have all of them at the same angular resolution. Therefore, we convolved all of them to the same circular beam. Because of the different weightings that

were tried, which affect the sensitivity and angular resolution of the images for the different wavelengths, we determined that the best circular beam to use was of a size of 50 mas, giving us a good compromise between resolution and SNR. Convolution was performed using the task `imsmooth` from `CASA`. In Figure 2.1 we show the final convolved images at each wavelength.

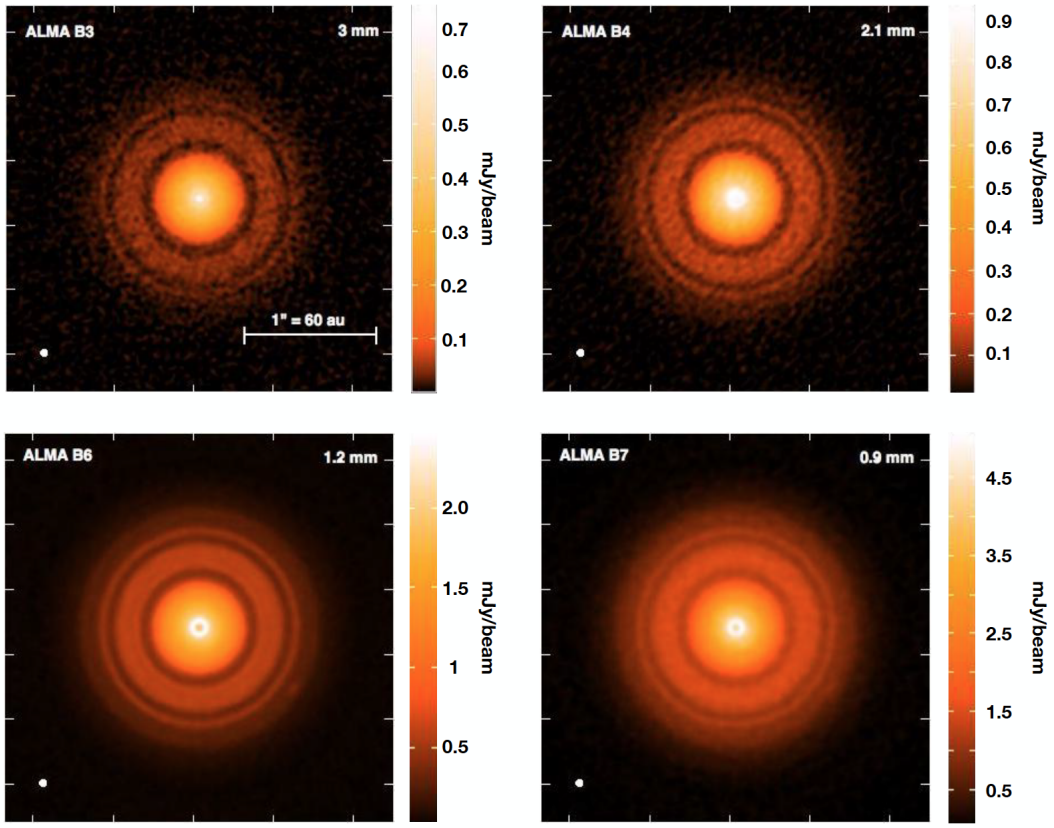

Figure 2.1: Set of final images for TW Hya. All images are convolved to the same beam with FWHM = 50 mas.

2.1.2 HD 163296

For HD 163296 we used ALMA data at 0.9 mm, 1.2 mm, 2.1 mm and 3 millimeters, the same as for TW Hya. Most of these data were downloaded from the ALMA archive, except the 1.2 millimeter data which was obtained already calibrated from the DSHARP project web page (Andrews et al. 2018a). For the archive observations, we followed the instructions from the reduction scripts to perform the calibration of the raw data using their corresponding version of `CASA`. Note that, in this case we used a single high resolution data set at each band to perform the analysis. There are some data sets covering shorter baselines but with very low SNR and very different frequencies than the high resolution observations. Thus, we decided to use one high resolution data set at each band for the analysis, where to ensure sensitivity at the same spatial scales we used a common uv-range of 33 to 5500 $k\lambda$ for all the observations.
Images were made using the task `tclean` of `CASA` and using the MSMFS algorithm. This time we used nterms = 1 because at each band we have only a single observation covering a narrow range of frequencies (see Table 2.1). We also used a pixel size of 0.1 times the major axis of the synthesized beam and scales of 0, 1, 3, 5 times the major axis of the synthesized beam. We used

the same robust parameter of 0.5 for all images and we convolved all to a circular beam of 102 mas. The final images are shown in Figure 2.2.

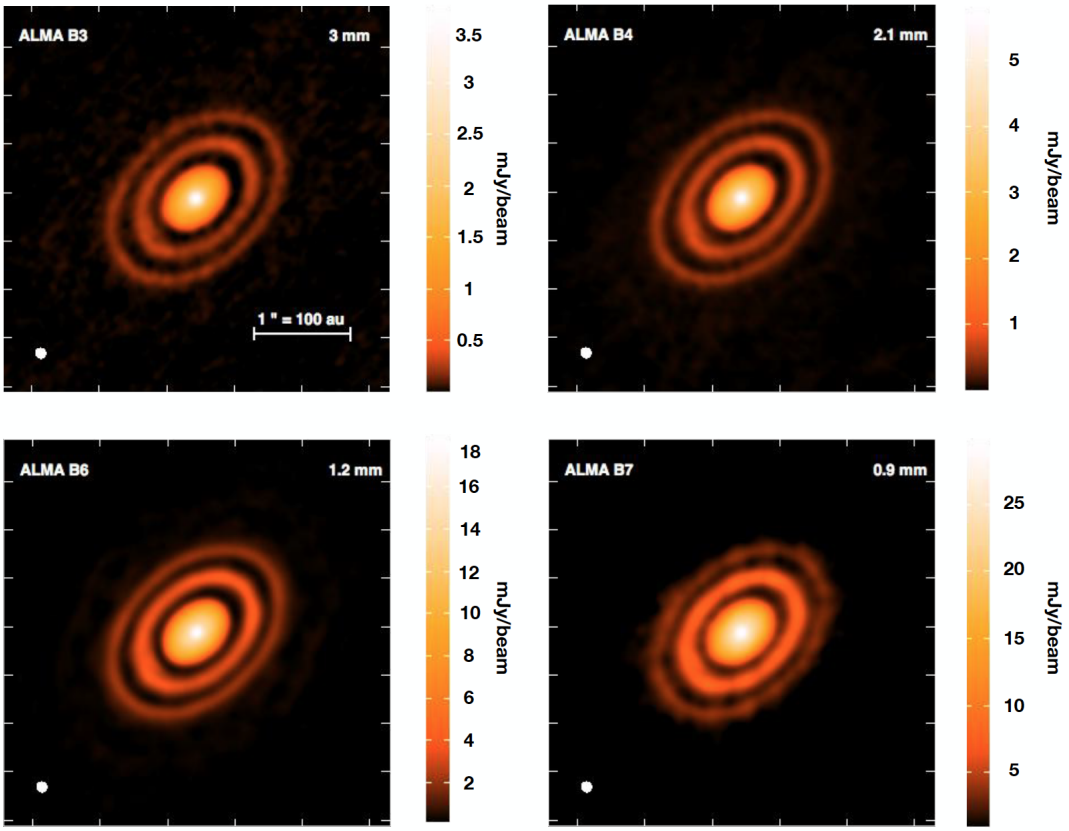

Figure 2.2: Set of final images for HD 163296. All images are convolved to the same beam with FWHM = 102 mas.

Table 2.1: TW Hya and HD 163296 Observations

Program	P.I.	Baseline Coverage (kλ)	ALMA Band	Frequency Coverage (GHz)
TW Hya				
2016.1.00229.S	E. Bergin	5.5 - 1013	3	97.8
2018.1.01218.S	E. Macías	26.9 - 5263	3	90.5 - 104.5
2015.A.00005.S	T. Tsukagoshi	8.2 - 5221	4	138 - 152
2016.1.00842.S	T. Tsukagoshi	8.7 - 7177	4	138 - 152
2015.1.00845.S	C. Favre	7.2 - 308	4	145
2015.A.00005.S	T. Tsukagoshi	12.6 - 8391	6	224 - 242
2016.1.00842.S	T. Tsukagoshi	11.6 - 870	6	224 - 242
2017.1.00520.S	T. Tsukagoshi	71.4 - 6638	6	224 - 242
2015.1.00686.S	S. Andrews	19.8 - 16736	7	344.5 - 357
2016.1.00629.S	I. Cleeves	17.1 - 4226	7	343
2016.1.00173.S	T. Muto	17.1 - 1598	7	336.5 - 350.5
HD 163296				
2016.1.01086.S	A. Isella	13.25 - 4373.6	3	95.99 - 107.98
2017.1.01682.S	G. Guidi	32.99 - 5340.6	4	133.98 - 145.96
2016.1.00484.L	S. Andrews	32.13 - 4778.5	6	232.58 - 246.88
2016.1.01086.S	A.Isella	21.84 - 4158.6	7	329.30 - 342.85

Table 2.2: TW Hya and HD 163296 Images

ALMA Band	Central Frequency (GHz)	Central Wavelength (mm)	Synthesized beam Major × minor (mas × mas)	P.A. (deg)	rms (μJy/beam)
TW Hya					
3	97.5	3.07	34 × 33	74	13
4	144.9	2.07	46×39	46	12
6	233	1.27	36×31	-85	9.5
7	346.7	0.87	36×28	73	26
HD 163296					
3	101.9	2.95	101×74	61	13.5
4	139.9	2.14	80×62	-53.5	13.3
6	239.7	1.25	56×47	88.5	25
7	336	0.89	70×61	89.3	101.5

2.2 Radial Profiles

In this work, we focus on the study of the dust properties along the radius from the central star in these two disks. For this, we analyze the spectral energy distribution (SED) at each radius in order to infer the average dust properties. Therefore, we obtained radial profiles of the intensity at each wavelength.

Radial profiles were obtained from the final images shown in the last section. The intensity at each band was extracted by averaging the emission from the images in elliptical rings, whose central position is the pick of the emission in the image and eccentricity and position angle were defined by the inclination and position angle of the disks. For TW Hya we used a i=7 °(Qi et al. 2004) and a P.A of 155° (Andrews et al. 2016), while for HD163296 we used an inclination of i=45° (Isella et al. 2007) and a P.A of 133° (Huang et al. 2018b). We used a width of 10 mas for the elliptical rings. Note that this width is five to ten times smaller than the beam of the observations. We used this value in order to have a good sample profile, although we actually cannot distinguish spatial scales smaller than the beam size. At each radius we assigned an

intensity equal to the average intensity within the ring and the error is given by:

$$\Delta I_\nu = \frac{rms_\nu}{\left(\frac{\Omega_{ring}}{\Omega_{beam}}\right)^{0.5}}, \tag{2.1}$$

where rms_ν is the rms noise of the image at a frequency ν and Ω_{ring} and Ω_{beam} are the solid angles of the ring and the synthesized beam, respectively.

We converted the intensity to brightness temperature using the full Planck equation.

$$I_\nu(T) = \frac{2h\nu^3}{c^2}\frac{1}{e^{\frac{h\nu}{kT}} - 1}. \tag{2.2}$$

The results for the brightness temperatures at each wavelength are shown in Figure 2.3 for TW Hya and 2.4 for HD 163296.

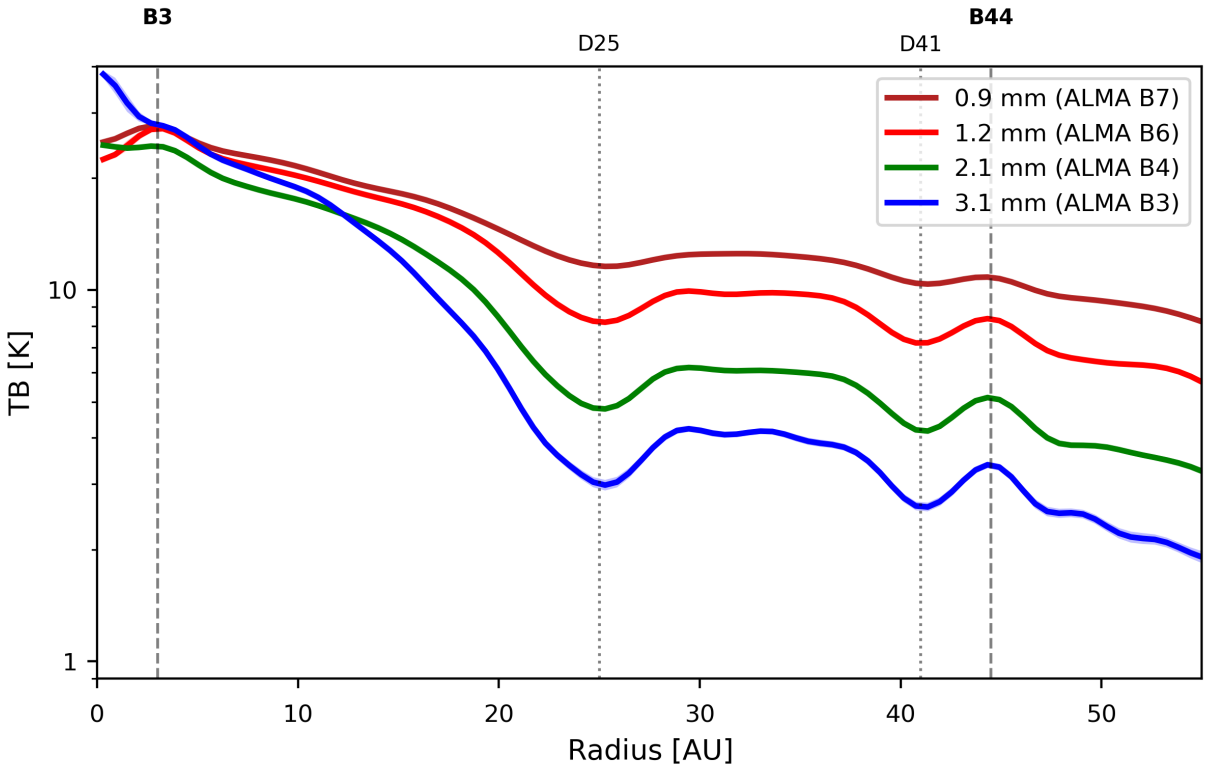

Figure 2.3: Brightness temperatures at each band for TW Hya.

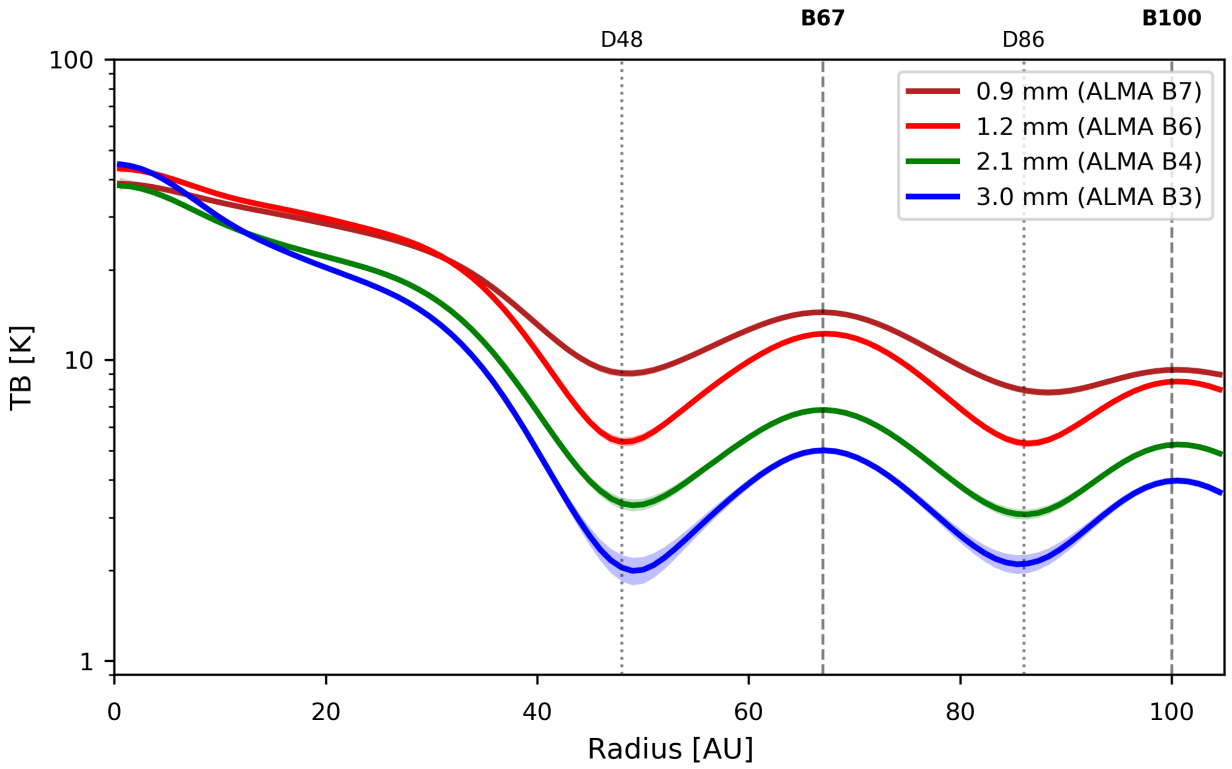

Figure 2.4: Brightness temperatures at each band for HD 163296.

Chapter 3

Modeling the dust particle distribution

In this work, the main objective is to analyze the images at each frequency to obtain the dust particle properties at each radius. Normally, the particle distribution at each radius of the disk is assumed to follow a power-law in the form:

$$n(a) \propto a^{-p} \quad ; \quad a_{min} < a < a_{max} \tag{3.1}$$

Where $\int_a^{a+da} n(a)da$ is the number of dust particles per unit volume with a size between a and $a + da$, and a_{min} and a_{max} are the smallest and the largest dust particles in the volume. The value of a_{min} is assumed to be $0.05\mu m$ and has little effect on the opacity at millimeter wavelengths. Meanwhile, the value of a_{max}, at least for the millimeter range, has a strong impact on the opacity of the emission. (e.g., Miyake & Nakagawa 1993).

For the case of dust evolution in the disk and formation of planets, the most interesting parameter to characterize is a_{max} since this can inform us about the size up to which the particles have grown at each radius.

In general, the behavior of the dust opacity with frequency is given by the extinction coefficient (χ_ν), which has a contribution from absorption and scattering,

$$\chi_\nu = \kappa_\nu + \sigma_\nu, \tag{3.2}$$

where κ_ν and σ_ν are the absorption and the scattering coefficients, respectively.

It is useful to the define the albedo as the fraction of the dust opacity which is consequence of scattering:

$$\omega_\nu = \frac{\sigma_\nu}{\kappa_\nu + \sigma_\nu}. \tag{3.3}$$

If the albedo is close to a value of 1, the scattering is dominating the dust opacity, while if ω_ν is close to 0, we can assume that the dust opacity is dominated by absorption. In Figure 3.1 we show the behavior in frequency and for different particle distributions of the three coefficients defined before.

As we can see from Figure 3.1, for different values of a_{max} we have different behaviors in the millimeter range of these coefficients. Then, by analyzing the behavior of the emission at different wavelengths we can, in principle, be capable of determining the maximum particle

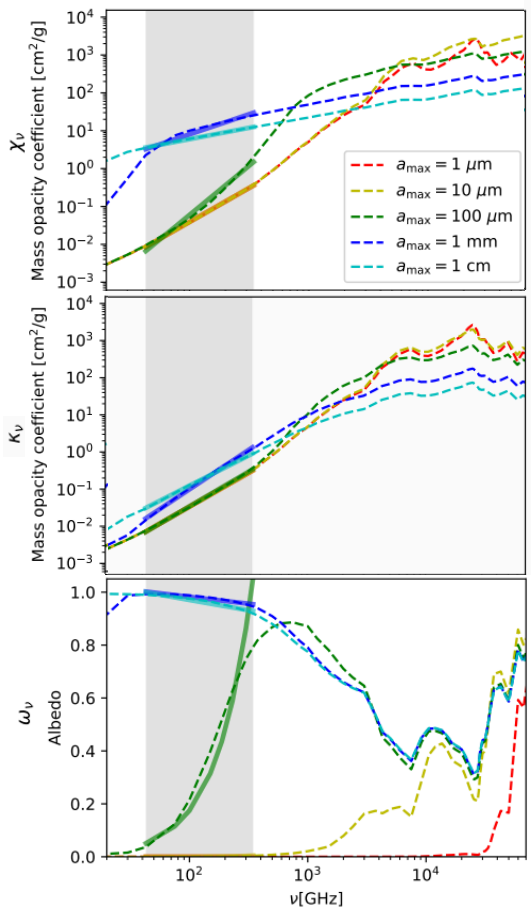

Figure 3.1: The spectral behavior of the extinction coefficient (χ_ν), the absorption coefficient (κ_ν) and the albedo (ω_ν), for particle sizes distribution with $p = 3.5$ and different values of a_{max}. Dust properties are computed using the (D' Alessio et al. 2001) code for compact spherical grains and a dust mixture of silicates ($\rho_{sil} = 3.3 gcm^{-3}$), organics ($\rho_{org} = 1.5 gcm^3$), and ice ($\rho_{ice} = 0.92 gcm^3$), with relative abundances of 26%, 31%, and 43% respectively (Pollack et al. 1994). The vertical grey areas in all panels mark the wavelength range between 1 mm and 1 cm. Color solid lines within the shaded frequency range are parametrizations of these coefficients as $\chi_\nu = \chi_0(\nu/\nu_0)^{\beta_\chi}$, $\kappa_\nu = \kappa_0(\nu/\nu_0)^{\beta_\kappa}$ and $\omega_\nu = \omega_0(\nu/\nu_0)^{\beta_\omega}$ adapted from (Carrasco-González et al. 2019).

size. Classically, the maximum particle size has been determined by using the spectral index between two wavelengths in the millimeter. However, this is only valid in the case of optically thin emission with the opacity being dominated by absorption and when this emission is in the Rayleigh-Jeans regime (see e.g, Carrasco-González et al. 2019 and Sierra et al. 2020). These assumptions are probably valid for the interstellar medium where low densities and small particles are expected, but in protoplanetary disks we expect higher densities and particle sizes close to the observing wavelength, so scattering becomes important (see Figure 3.1). In the following, we describe how to obtain the dust parameters through sub-mm observations. First, we explain the classical method assuming optically thin emission and only absorption. Then, we explain a more general method that takes into account also scattering and no assumption about the optical depth of the emission. In this work, we used the method including scattering

and absorption which requires several wavelengths covering a wide range of frequencies.

3.1 Absorption-only approximation

If we consider a disk in which opacity is dominated only by absorption, and we assume that at each radius the disk is isothermal, we can write the SED of the dust emission at each radius as,

$$I_\nu = S_\nu[1 - \exp(\tau_\nu)], \tag{3.4}$$

where I_ν is the emergent intensity, S_ν is the source function and τ_ν is the optical depth at the observed frequency. In this case, the τ_ν only depends on the absorption coefficient,

$$\tau_\nu = \Sigma_{dust}\kappa_\nu, \tag{3.5}$$

where Σ_{dust} and κ_ν are the dust surface density and the absorption coefficient respectively.

At millimeter wavelengths the absorption coefficient approximately follows a power-law (see Figure 3.1).

$$\kappa_\nu = \kappa_0 \left(\frac{\nu}{\nu_0}\right)^\beta. \tag{3.6}$$

Therefore, if we consider optically thin emission, $\tau_\nu \ll 1$, then

$$I_\nu \simeq B_\nu(T)\tau_\nu \propto B_\nu \nu^\beta, \tag{3.7}$$

where τ_ν is $\Sigma_{dust}\kappa_\nu$ which will lead to $\tau_\nu \propto \nu^\beta$ due to the power-law behavior of κ_ν. If we consider we are in the Rayleigh-Jeans regime ($h\nu \ll kT$) we can approximate $B_\nu \propto \nu^2$. Therefore, in the optically thin case we can assume that the specific intensity, $I_\nu \propto \nu^{2+\beta}$, i.e., the spectral index of the emission is related to β, as $\alpha = 2+\beta$. Therefore, by observing at two wavelengths in the millimeter range, we can obtain β from the spectral index and then estimate the maximum particle size (See Figure 3.2).

Recent ALMA observations have revealed that disks are not always optically thin at wavelengths < 3 millimeters (e.g., Liu et al. 2017; Huang et al. 2018b). Considering that the emission is optically thin when it is not leads to an overestimation of the particle sizes and the underestimation of the disk's mass (Carrasco-González et al. 2019; Galván-Madrid et al. 2018) (see Figure 3.2). Moreover, in protoplanetary disks we expect dust to have grown to millimeter sizes, then, we expect very high values of the albedo. Therefore, this method in general could not be valid for most protoplanetary disks (Sierra et al. 2019; Zhu et al. 2019).

3.2 Scattering + absorption

As commented above, protoplanetary disks are expected to have millimeter- or even centimeter-sized particles, then, high values of albedo at millimeter wavelengths are expected , and the dust opacity is most probably totally dominated by scattering. If scattering is important, the spectral index between two wavelenghts is not easily related to the dust particle properties anymore (e.g., Sierra et al. 2020; Zhu et al. 2019). To properly analyze the SED for protoplanetary disks, we need to take into account both effects for the dust opacity, absorption and scattering. This will cause the shape of the SED to be related to the spectral behavior of the extinction coefficient, not by the spectral behavior of the κ_ν.

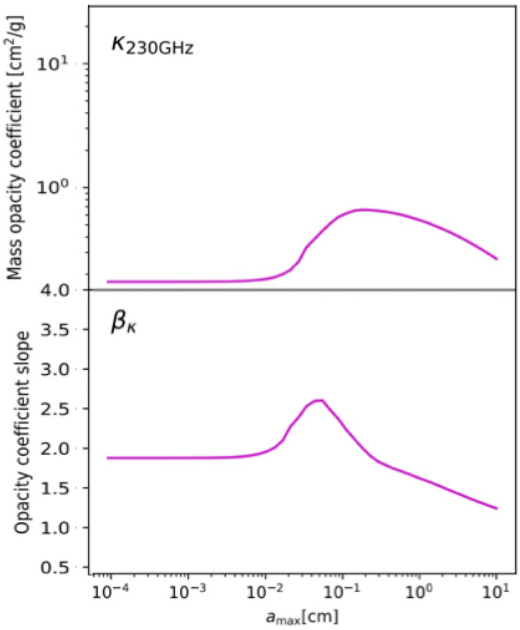

Figure 3.2: Dependence with a_{max} of the absorption coefficient at a reference frequency of 230 GHz. The bottom panel show the values of the slopes describing the spectral variation of the coefficient with a_{max} (Carrasco-González et al. 2019).

In order to include the scattering effect, we can write the source function in the radiative transfer equation as:

$$S_\nu(T) = \omega_\nu J_\nu + (1 - \omega_\nu) B_\nu(T), \tag{3.8}$$

where J_ν is the local mean intensity. We can approximate this to the analytical solution found in Miyake & Nakagawa 1993 assuming a disk as a vertically isothermal slab and with isotropic scattering:

$$J_\nu = B_\nu(T)[1 + f(t, \tau_\nu, \omega_\nu)], \tag{3.9}$$

where

$$f(t, \tau_\nu, \omega_\nu) = \frac{\exp(-\sqrt{3}\epsilon_\nu t) + \exp(\sqrt{3}\epsilon_\nu(t - \tau_\nu))}{\exp(-\sqrt{3}\epsilon_\nu \tau_\nu)(\epsilon_\nu - 1) - (\epsilon_\nu + 1)}, \tag{3.10}$$

where t is the variable optical depth, $\tau_\nu = \Sigma_{dust}\chi_\nu$, both are measured perpendicular to the disk mid plane, and $\epsilon_\nu = \sqrt{1 - \omega_\nu}$. Considering inclination effects by correcting the optical depth by the inclination angle (i) of the disk, we reach the emergent specific intensity obtained by Sierra et al. 2019:

$$I_\nu = \int_0^{\tau_\nu/\mu} S_\nu(T) e^{-t/\mu} \frac{dt}{\mu} = B_\nu(T)[(1 - \exp(-\tau_\nu/\mu)) + \omega_\nu F(\tau_\nu, \omega_\nu)]. \tag{3.11}$$

Integrating along τ_ν/μ, where $\mu = \cos(i)$, it is found

$$F(\tau_\nu, \omega_\nu) = \frac{1}{\exp(-\sqrt{3}\epsilon_\nu \tau_\nu)(\epsilon_\nu - 1) - (\epsilon_\nu + 1)} \text{x}$$
$$\left[\frac{1 - \exp(-(\sqrt{3}\epsilon_\nu + 1/\mu)\tau_\nu)}{\sqrt{3}\epsilon_\nu \mu + 1} + \frac{\exp(-\tau_\nu/\mu) - \exp(-\sqrt{3}\epsilon_\nu \tau_\nu)}{\sqrt{3}\epsilon_\nu \mu - 1}\right]. \tag{3.12}$$

It is important to note that these equations assume isotropic scattering, which may be a incorrect approximation for $2\pi a \geqslant \lambda$. To reduce the effect of the approximation, it is necessary to replace the scattering coefficient in all equations by an effective scattering coefficient in the form (Ishimaru 1978, Birnstiel et al. 2018) :

$$\sigma_{\nu}^{eff} = (1 - g_{\nu})\sigma_{\nu}, \tag{3.13}$$

where g_{ν} is the asymmetry parameter, i.e., the expectation value of $\cos\theta$, where θ is the scattering angle (e.g. Ishimaru 1978, Birnstiel et al. 2018). The values of g_{ν} depend on the dielectric properties of the dust particles. We used the values of σ_{ν}^{eff} obtained in Birnstiel et al. (2018).

Although equations 3.11 and 3.12 seem complicated, note that they only depend on four free parameters: dust temperature (T), the surface density (Σ_{dust})and the two parameters that define the particle distribution (a_{max} and p). If we fix a value for p (i.e. a typical value of 3) then, with three wavelengths or more, we should be able to obtain the three free parameters that are left (T, Σ_{dust}, a_{max}). It is important to mention that this model assumes that at each radius the disk has a single temperature. This is a good approximation in the case that most of the dust is settled in the disk mid plane.

This kind of analysis was performed for the first time on HL Tau using four images between 8 mm and 0.9 mm (Carrasco-González et al. 2019). However, in that work the spectral behavior of the extinction coefficient was simplified by a power-law for convergence issues. In this work, we avoid this approximation and we used the exact values of the dust opacity at each wavelength.

3.3 Dust parameters degeneracy problem

Note that there is an important degeneration in the dust opacity. This is due to the fact that the optical depth is the product of the dust surface density and the extinction coefficient that depends of a_{max}. Then, at a given wavelength an increment of the optical depth can be explained by an increment in density or a change in a_{max}. Therefore, almost in any case we will have two possible solutions: A solution with high densities and small particles, and another with low densities and large particles. In order to alleviate this degeneracy problem, we need to include in our analysis the widest range of frequencies possible. For example, if large particles are present, we expect to have important emission at long wavelengths while if not, then, the SED can only be explained with small particles. In addition, another important difference between the two solutions is the temperature. Therefore, if one has a shorter wavelength observation, this parameter can be better constrained, making it possible to discern between the two solutions. To give a more detailed view of the degeneracy problem that is faced, we created a synthetic SED with fixed values for the dust parameters. We calculated the intensity values for wavelengths normally found in data sets for ALMA and the VLA in these synthetic SED and then we fitted this with different guesses for dust particle size parameter and different combinations of wavelengths. We show the results in Figure 3.3.

From this figure it is clear that, in order to break the degeneracy between the different parameters in the SED, long wavelength observations are fundamental. Note however, that observations at these wavelengths are very difficult to perform at the present moment with the current instruments. In particular for our study, we only have observations up to 3 millimeters, and we expect to have a large degeneracy. We will always consider both solutions, small and large particles, and decide which is the most likely using other arguments.

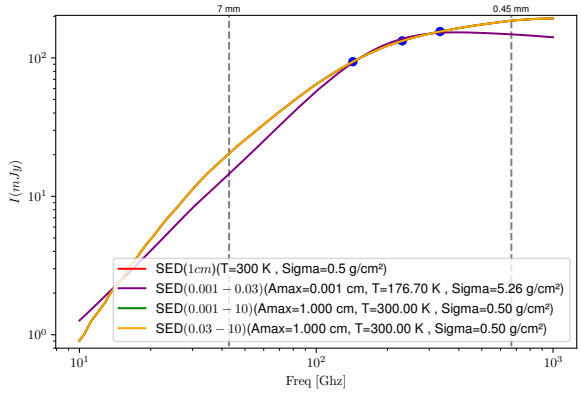

(a) SED's for 0.9,1.2,2.1 millimeters

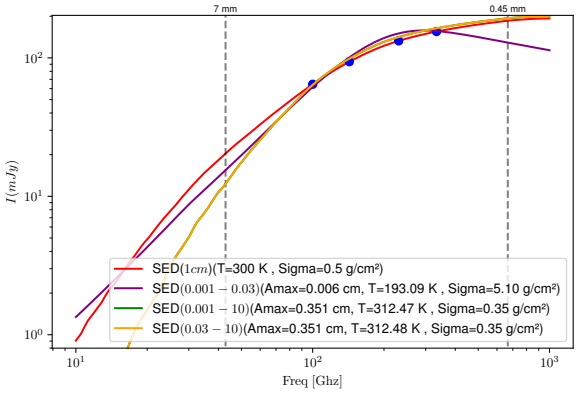

(b) SED's for 0.9,1.2,2.1,3 millimeters

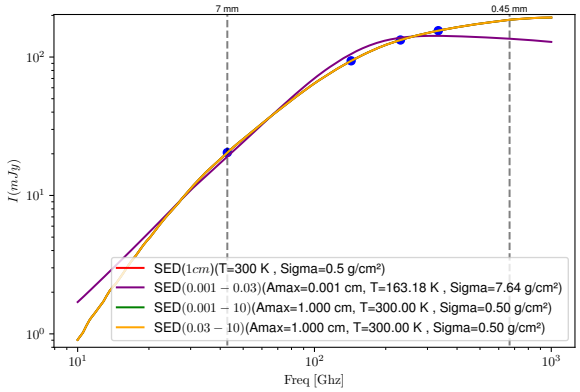

(c) SED's for 0.9,1.2,2.1,7 millimeters

Figure 3.3: (a) SED's from the dust emission using the intensity at 0.9, 1.2 and 2.1 millimeters obtain from the synthetic SED to do the fitting: the red line shows the synthetic SED for a particle size of 1 centimeter, temperature of 300 K and a surface density of 0.5 g/cm^2. For the other 3 color lines (yellow, purple and green) we took the intensity values for wavelengths normally found in data sets for ALMA and the VLA from the synthetic SED to be able to perform three fittings of the dust parameters with different ranges of values as guesses for the particle size: purple (0.001-0.03 cm), green (0.03-10 cm) and yellow (0.001-10 cm). (b) SED's from the dust emission using the intensity at 0.9, 1.2, 2.1 and 3 millimeters. (c) SED's from the dust emission using the intensity at 0.9, 1.2, 2.1 and 7 millimeters. Note that almost every time the yellow line behaves exactly as the red and the green line which is why they aren't seen in all the plots.

3.4 Analysis

In order to obtain the physical parameters of the dust properties at each radius we compare the values of intensity with the expected SED from different combinations of the three free parameters. We fix a value for p in the particle size distribution. For protoplanetary disks it is commonly assumed that p is equal to that of the interstellar medium (Mathis et al. 1977). However, no actual result has supported this completely, at least for gaseous protoplanetary disks. Alternatively, several recent studies using dust evolution models have shown that it is more likely for this slope to take values a little bit flatter (i.e., dust particle size distributions with more large particles; Drazkowska et al. 2019). This is also intuitive, if the disks are formed from the interstellar medium with a p = 3.5 then, grain growth in the earliest stages of the formation of the disk should lead to flatter values of the slope of this particle distribution. This

is also supported by the high values of the visual extinction observed near young stellar objects which suggest a particle distribution with larger grains than in the ISM (e.g. Hernández et al. 2004). Therefore, we decided to use a value slightly below than that of the ISM, we used p=3. We use the DSHARP opacities explained in Birnstiel et al. (2018), which use particles without porosity and a composition of 20 % water fraction by mass, 32.91 % astronomical siliticates, 7.43 % troilite and 39.66 % refractory organics.

We explored different combinations for the three free parameters in equation 3.12 (a_{max},T_{dust},Σ_{dust}). We adopted a Bayesian approach to obtain the posterior probability distributions of the model parameters at each radius. We use a standard log-normal likelihood function defined as:

$$\ln p(\bar{I}(r) \mid \Theta) = -0.5 \sum_i \left((\frac{\bar{I}_i - I_{m,i}}{\hat{\sigma}_{\bar{I},i}})^2 + \ln(2\pi\hat{\sigma}^2_{\bar{I},i}) \right), \tag{3.14}$$

where $\bar{I}$ is the azimuthally averaged intensity at radius r and at frequency ν_i, $I_{m,i}$ is the model intensity obtain from different combinations of the three free parameters at a radius r, Θ is the three free parameters vector and assuming that the uncertainty $\hat{\sigma}_{\bar{I},i}$ at radius r is:

$$\hat{\sigma}_{\bar{I},i} = \sqrt{\sigma^2_{\bar{I},i} + (\delta_i \bar{I}_i)^2}, \tag{3.15}$$

where $\sigma^2_{\bar{I},i}$ is the error of the mean obtained from the azimuthally averaged intensity profiles explained in the observations chapter, and δ_i is the absolute flux calibration error at each frequency. We set this systematic error to the nominal values of 10% at Band 7, and 5% at Bands 6, 4, and 3 for the two disks.

We created a grid of intensities with different dust parameters using the data mentioned before. We fitted the spectral energy distribution (SED) of the millimeter emission coming from the observations at each radius by showing the probability distribution of each parameter that better fulfill the conditions of the observational data.

In addition, we put a constraint in the temperature parameter to remove the unrealistic high values showing at the outer radii of the protoplanetary disks analyzed (TW Hya and HD 163296). We used a Gaussian prior centered at the temperature profile for a passively irradiated disk, which approximates the mid-plane temperature profile with the simplified expression for a passively heated, flared disk in radiative equilibrium as (Dullemond et al. (2018):

$$T_{mid}(r) = \left(\frac{\phi L_*}{8\pi R^2_{disk} \sigma_{SB}} \right)^{0.25}, \tag{3.16}$$

where σ_{SB} is the Stefan-Boltzmann constant and is defined as $\sigma_{SB} = \frac{2\pi^5 k_b^4}{15h^3c^2} = 5.670 \times 10^{-8}$, L_* is the stellar luminosity and ϕ is the flaring angle. We select the value for $\phi \simeq 0.02$ for both disks (TW Hya and HD 163296) because it is a conservative value and it is consistent with the analysis in Dullemond et al. (2018), which treats the effect of the assumed temperature profile on other derived disk properties in more detail. Finally, we assume the Gaussian prior defined as:

$$f(x) = \frac{1}{\sigma\sqrt{2\pi}} e^{-\frac{1}{2}(\frac{x-\mu}{\sigma})^2}, \tag{3.17}$$

where σ is the standard deviation, μ is the temperature profile obtain with equation 3.17 and x is the total range of temperatures define in the grid in the analysis. To try not being very

restrictive with the width of the prior and obtain additional temperature information, we used different widths and found at that a standard deviation equal to 50% and 30% of the central value for TW Hya and HD 163296 respectively, was really good to achieve the results we wanted.

Chapter 4

Results and discussion

In this chapter we present the results obtained from the procedure described in chapters 2 and 3 for TW Hya and HD163296. At the beginning of each section we also give a short introduction of each object.

4.1 TW Hya

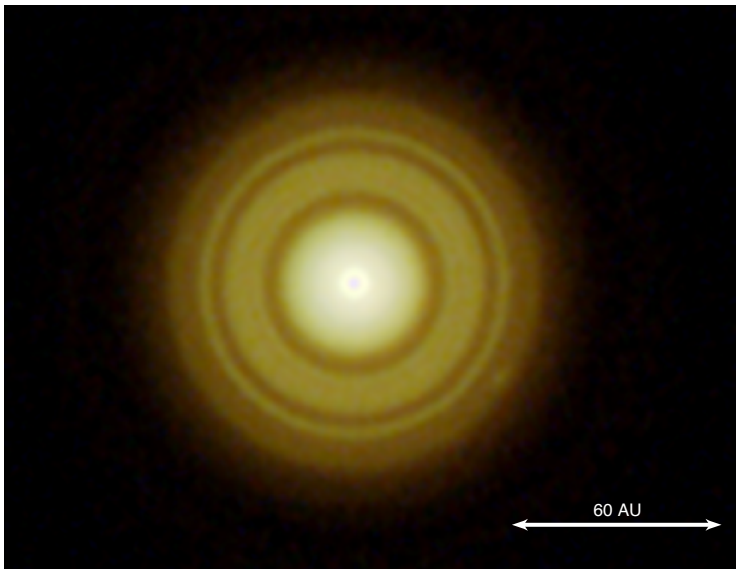

Figure 4.1: RGB Image of TW Hya: In red 0.9 millimeters is shown, in green 1.2 millimeters and in blue 3 millimeters.

TW Hya is a T Tauri star with a mass of 0.6 $M_{\odot}$ surrounded by a disk at a distance of 59.5 pc (Gaia Collaboration et al. 2016) and a stellar age of 10 Myr (Andrews et al. 2012). It has a disk inclination of 7 °, almost completely face-on (Qi et al. 2004), an accretion rate of 4x10^{-10} M$\odot$ yr^{-1} (Muzerolle et al. 2001) and it is considered to be an excellent target to study the radial particle distribution due to its proximity and orientation. High-resolution ALMA observations have previously revealed a couple of gaps at 25 and 41 au and two rings at 3 and 44 au (Andrews et al. 2016; Tsukagoshi et al. 2016; Huang et al. 2018a)(see Figure 4.1). It is a relatively massive disk for its age (> 0.05 $M_{\odot}$) as inferred from HD line observations (Bergin et al. 2013) which, considering a reasonable gas-to-dust ratio, we can assume that large concentrations of dust particles are still present in the disk. Many studies using high angular resolution ALMA

observations (0.9 mm,1.2 mm and 2.1 mm) proposed that the gaps and rings could be formed by different scenarios such as planet disk interaction, zonal flows and snowlines (Andrews et al. 2016; Tsukagoshi et al. 2016; Nomura et al. 2016). The radial properties of the dust have been studied only by using spectral index and considering absorption only (e.g Huang et al. 2018a and Tsukagoshi et al. 2016). These studies revealed high contrast between gaps and rings, higher values of the spectral index in gaps and constrained the grain sizes to a few millimeter. They also found low spectral index values in the rings which they associated to be centimeter size grains, but they could not exclude optically thick emission. More recently, (Tsukagoshi et al. 2019) found an excess in the dust continuum emission (1.2 millimeters) at 52 au in TW Hya (see Figure 4.1). They explained this feature as a weak gas vortex due to his lower over-density with his surroundings, but they also said this excess could be related with the presence of a low mass planet. In this work, for the first time we analyze all the available observations in order to obtain the dust distribution considering absorption and scattering.

We explore a temperature range from 0.1 to 100 K and a Σ_{dust} range from 0.001 to 1000 g/cm^2. For the large particles solutions we explore a_{max} from 200 μm to 10 cm and for the small particles solution we explore $a_{max} < 200$ μm. For the temperature profile prior we use a L_* of 0.23 $L_\odot$ (Sokal et al. 2018) and an inclination of 7° to correct for the disk geometry. In Figure 4.3 we show the results of our simple model for both solutions. We can note that at the inner radii (< 20 au) our fit of the observed intensity profiles (see Figure 4.2) is worse than at the outer radii (> 20 au). One reason for the behavior of the dust parameters at the inner regions is that these have extremely high optical depths. This can't produce good results since we need in our analysis a variety of optical depths at different wavelengths. Moreover, it has been also proposed that emission at short radii can be contaminated with free-free emission (Wilner et al. 2005; Gorti et al. 2011; Menu et al. 2014). A proper analysis will need to decontaminate for free-free emission in order to obtain better results.

The small particles solution presents different characteristics in the dust parameters: First, we can see that temperature does not match the passively irradiated disk solution, leading to an unrealistic cold disk (T < 20 K from r > 10 au). We can also see that the surface density decreases with radius as expected, but it shows a high total integrated dust mass > 0.014 $M_\odot$. This would probably result in a highly gravitationally unstable disk if one assumes a commonly used gas-to-dust ratio in the range of a 100 and 10. To support this we calculated the density profiles for a Toomre parameter equal to 1 in both disks, using (see Figure 4.3 and 4.6):

$$Q = \frac{c_s \Omega_K}{\pi G \Sigma_g}, \tag{4.1}$$

where $c_s = \sqrt{k_B T/\mu m p}$ is the sound speed, $\Omega_K = \sqrt{G M_\star / r^3}$ is the Keplerian frequency, and Σ_g is the gas surface density, we assume a gas-to-dust ratio of a hundred and ten times the dust mass. Solutions with higher densities than this curve are gravitationally unstable.

Finally, note that the particle size tends to always reach the upper limit that we imposed for these solution, suggesting that larger particles are necessary in order to explain the SED. For all of this reasons, we decided to discard the results from the small particle solution (see Figure 4.3).

For the large particle solution we found that the temperature is close to the passively irradiated disk solution. For r > 20 au we obtained surface densities in the range from a few 10^{-1} to $\simeq 5{\times}10^{-2}$ g/cm^2 and a particle size a bit larger than 1 millimeter. One of the most important result from the analysis is that the substructures that are noted in TW Hya show some contrast

in intensity, particle size and density. This contrast means that the dark rings (D25, D41) seem to have lower density and smaller particles than its surroundings, while the bright rings (B44) displays higher densities and larger particles sizes. It is important to note that this contrast can still be affected by our resolution (50 mas), so the actual difference in the dust parameters between gaps and rings is probably larger than we see.

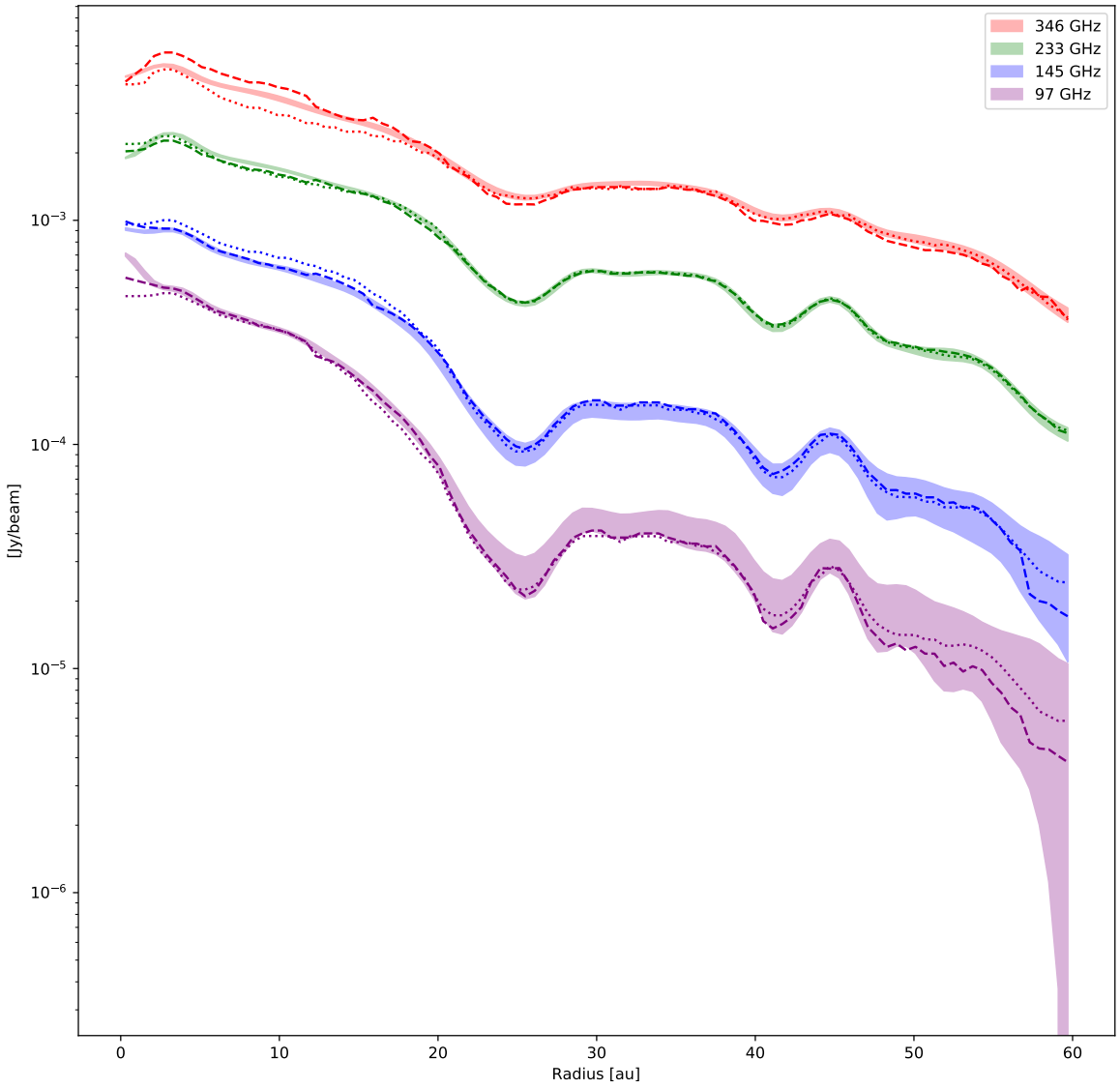

Figure 4.2: Intensity radial profiles for TW Hya at the 4 different wavelengths used in the analysis at 346 GHz (B7, 0.9 millimeters), 233 GHz (B6, 1.2 millimeters) , 145 GHz (B4, 2.1 millimeters) and 97 GHz (B3, 3 millimeters). The color zones show the intensity profiles obtained from the observational data with the errors for each of the wavelengths, while the dashed lines and the dotted lines display the intensity radial profiles found in the fitting of the dust parameters for the large and small particle solutions, respectively.

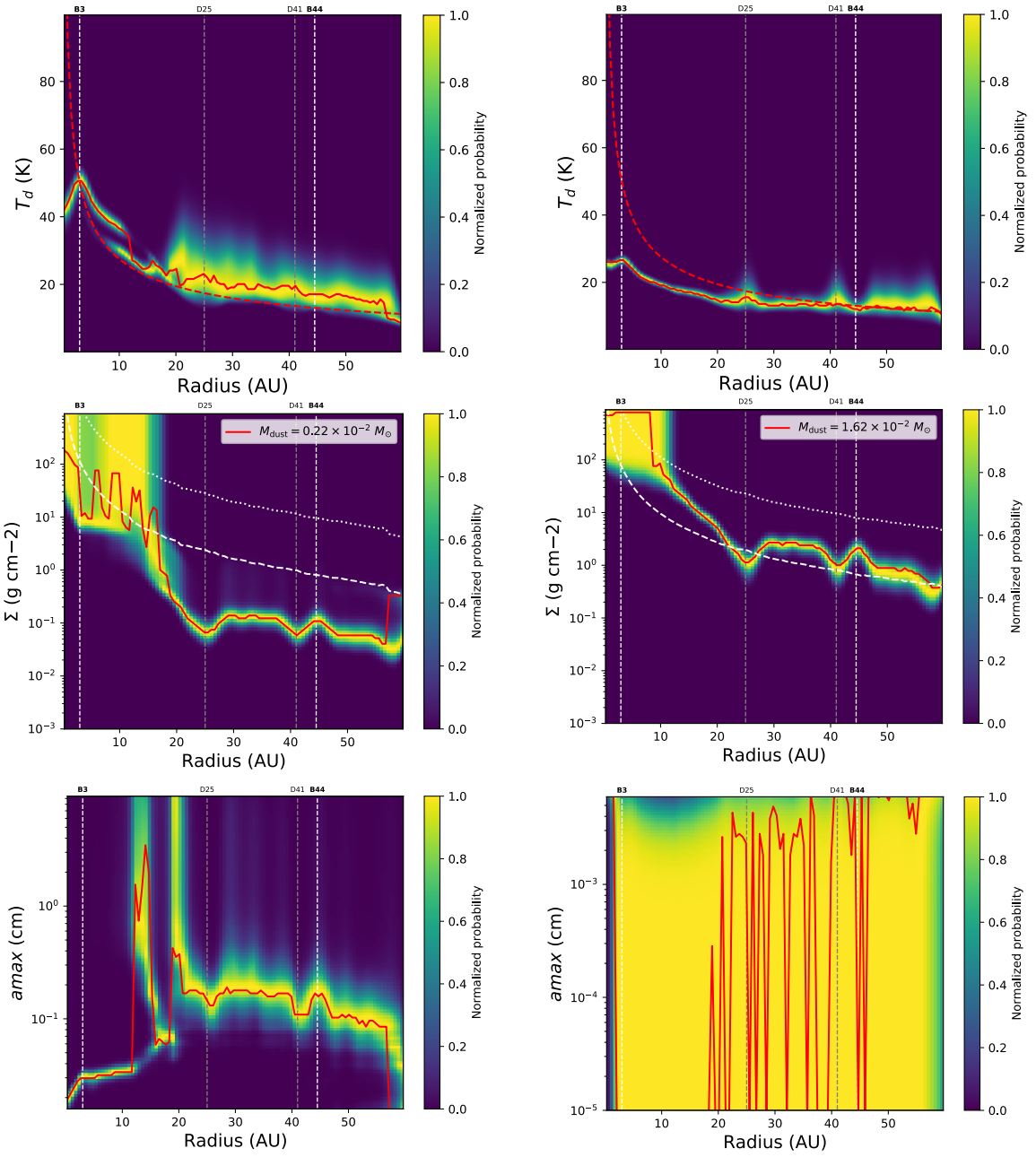

Figure 4.3: In yellow we show the probability distributions of each parameter fitted to the multi-wavelength observations. The posterior probabilities are normalized by the maximum marginalized probability at each radius to make them easier to understand. *Left*: Normalized temperature, surface density and maximum particle size for the large particle solution. *Right*: Normalized temperature, surface density and maximum particle size probability for the small particles solution.The red dashed line in the top figures displays the temperature profile obtained from a passively irradiated disk for both solutions. In the middle plots we also show an estimate for the disk dust mass and the dust surface density profiles as the white dashed and dotted lines for which the Toomre Q parameter equals 1 with a gas-to dust ratio of 100 and 10, respectively. The red solid lines in all plots indicate the maximum posterior probability for each parameter at each radius. We display the known gaps (D) and rings (B) for TW Hya the gray and the white vertical lines respectively.

4.2 HD 163296

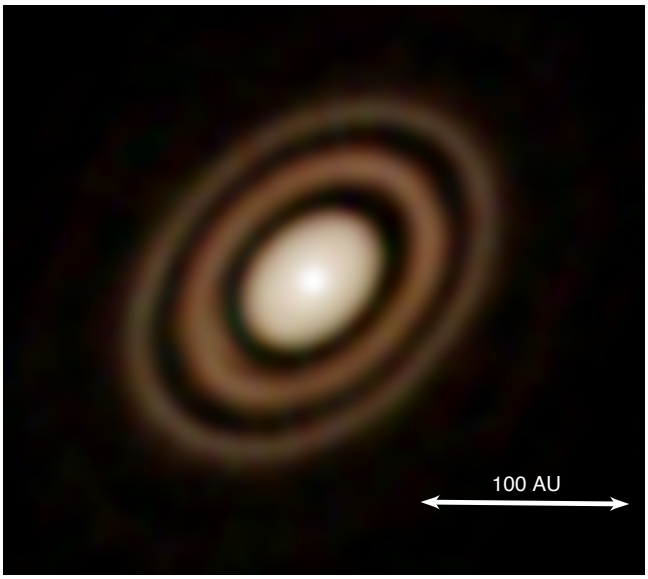

Figure 4.4: RGB Image of HD 163296: In red 1.2 millimeters is shown, in green 2.1 millimeters and in blue 3 millimeters.

HD 163296 is a Herbig Ae star with a mass around 1.9 $M_\odot$ (Setterholm et al. 2018) and a relatively large circumstellar disk ($\simeq$ 100 au) with an estimated age of 5 Myr (Montesinos et al. 2009) and an accretion rate of 4.5x10^{-7} $M_\odot$ yr^{-1}(Mendigutía et al. 2013) located at a distance of 101 pc (Gaia Collaboration et al. 2018). The mass of the disk has been estimated to be 0.01 to 0.15 $M_\odot$ (Isella et al. 2007; Muro-Arena et al. 2018; Tilling et al. 2012). The inclination of the disk was inferred to be 45° (Isella et al. 2007) and ALMA observations resolved the gas and dust emission, finding four dark (15, 45, 87 and 140 au) and three bright (68, 100 and 160 au) rings (Isella et al. 2016; Isella et al. 2018; Zhang et al. 2016). A study of the total SED of the disk at different wavelengths suggested the presence of centimeter size particles in the mid plane of the disk and an important contribution from free-free emission at long wavelengths (Isella et al. 2007). Finally, the asymmetric substructure in the dust continuum emission in second ring of the disk lead to the conclusion that HD 163296 is being affected by the gravitational interaction of unseen planets (Isella et al. 2018).

We explored a temperature range from 0.1 to 100 K and a Σ_{dust} range from 0.001 to 1000 g/cm^2. For the large particles solutions we explore a_{max} from 200 μm to 10 cm and for the small particles solution we explore $a_{max} < 200$ μm. For the temperature profile prior we use a L_* of 17 $L_\odot$ (Andrews et al. 2018a) and an inclination of 45° to correct for the disk geometry. In Figure 4.6 we show the results found for HD 163296. As in TW Hya, we see a problem of high optical depth at the inner radii (r < 40 au)(see Figure 4.5). Note that this implies a much larger optically thick region that in the case for TW Hya, this is probably a consequence of HD 163296 been younger and more massive than TW Hya.

The small particles solution shows a temperature that is very far from the passively irradiated disk solution, making the disk unrealistically cold (T < 20 K from r > 25 au). The high surface densities seen in the small particle solution will also probably end up in a highly gravitationally unstable disk for a range of gas-to-dust ratio of a 100 and 10, as we mentioned

for TW Hya (as evidenced by the high integrated dust mass > 0.01 $M_{\odot}$ and the surface density being higher than the densities for which Toomre parameter=1) (see Figure 4.6). We also choose to discard this solution.

In the large particle solution we see a temperature gradient close to the passively irradiated disk solution and a range of surface densities from $\simeq 10^{-1}$ to $\simeq 10^{-2}$ g/cm^2. We estimated particle sizes of a few millimeter for radii > 40 au. Furthermore, we also see that the dark rings (D49, D85) seem to have lower density and smaller particles, while the bright rings (B67, B100) display higher densities and larger particles sizes. Note that in this case the contrast between dark and bright rings is of an order of magnitude larger in density. It is also worth noting that at 100 au we found a ring which seems to be accumulating very large particles.

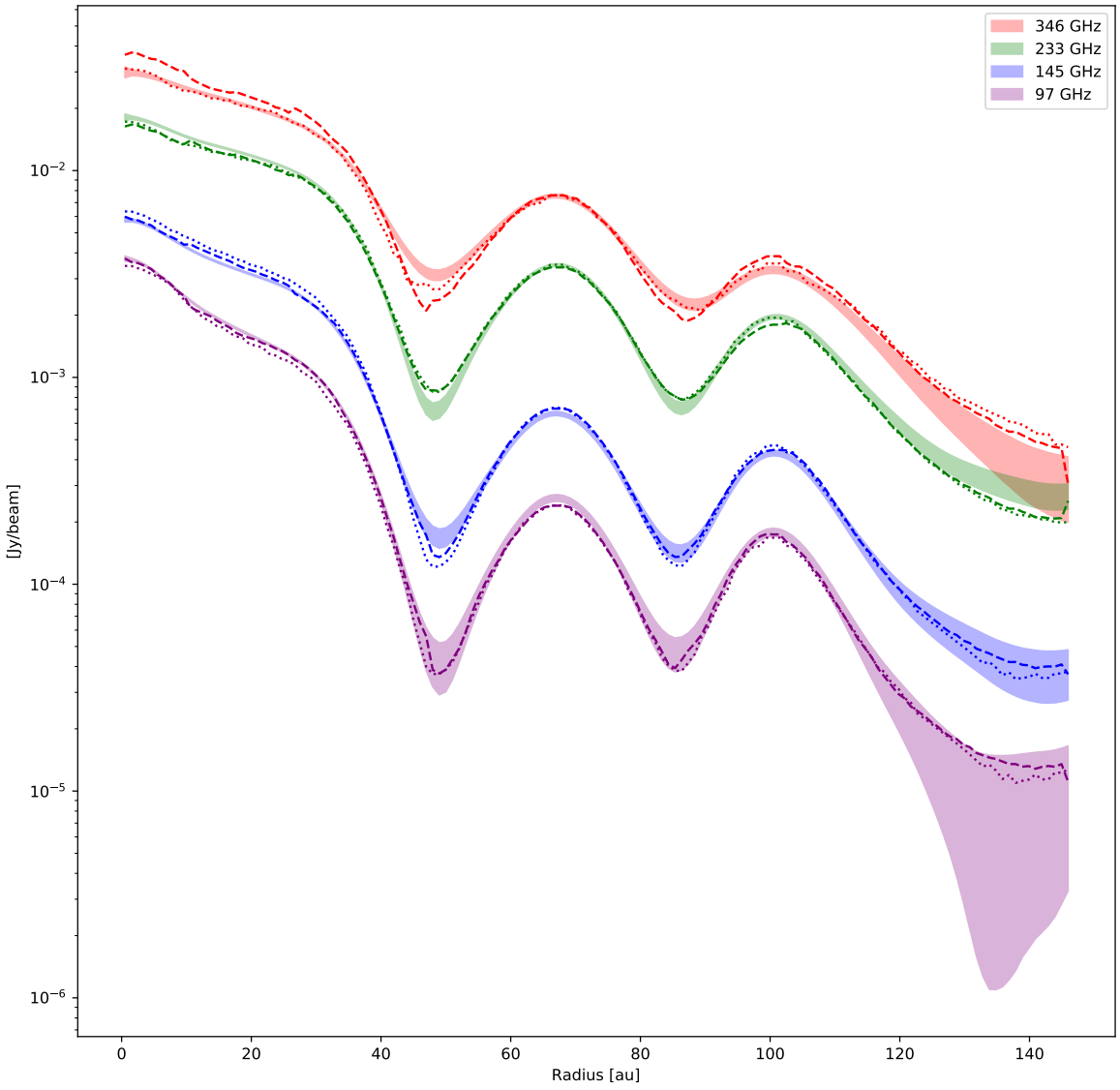

Figure 4.5: Intensity radial profiles for HD163296 at 4 different wavelengths used in the analysis at 346 GHz (B7, 0.9 millimeters), 233 GHz (B6, 1.2 millimeters) , 145 GHz (B4, 2.1 millimeters) and 97 GHz (B3, 3 millimeters). The color zones show the intensity profiles obtained from the observational data with the errors for each of the wavelengths, while the dashed lines and the dotted lines display the intensity radial profiles found in the fitting of the dust parameters for the large and small particle solutions, respectively.

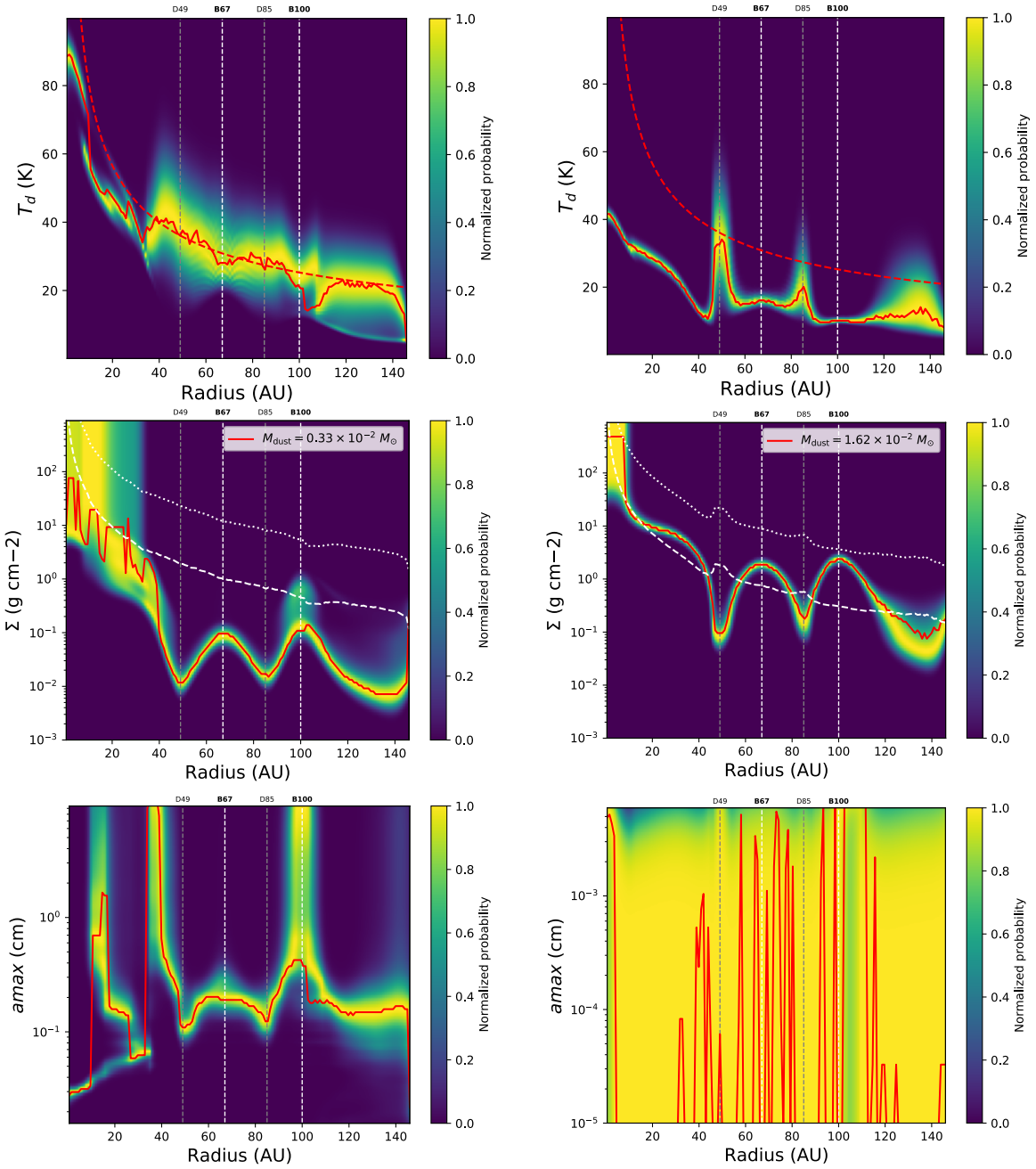

Figure 4.6: In yellow we show the probability distributions of each parameter fitted to the multi-wavelength observations. The posterior probabilities are normalized by the maximum marginalized probability at each radius to make them easier to understand. *Left*: Normalized temperature, surface density and maximum particle size for the large particle solution. *Right*: Normalized temperature, surface density and maximum particle size probability for the small particles solution.The red dashed line in the top figures displays the temperature profile obtained from a passively irradiated disk for both solutions. In the middle plots we also show an estimate for the disk dust mass and the dust surface density profiles as the white dashed and dotted lines for which the Toomre Q parameter equals 1 with a gas-to dust ratio of 100 and 10, respectively. The red solid lines in all plots indicate the maximum posterior probability for each parameter at each radius. We display the known gaps (D) and rings (B) for HD 163296 the gray and the white vertical lines respectively.

Chapter 5

Summary, general discussion and conclusions

In this work we present a multi-wavelength analysis of high angular resolution ALMA images. For this, we used high sensitivity images at 0.9, 1.2, 2.1 and 3 millimeter with an angular resolution of 50 mas and 102 mas for TW Hya and HD 163296, respectively. These images allowed to detect substructures at scales <= 10 au. We perform a basic analysis of the spectral energy distribution at each radius in order to obtain dust physical properties. For this we used an analytic solution of the radiative transfer equation for a thin disk with constant vertical temperature, densities and particle distribution. Our model includes absorption and scattering in the dust opacity which is important if large particles (millimeter or centimeter sizes) are present in the disk.

This type of analysis are important because we obtain physical parameters of the radial particle distribution. In addition, these studies with high angular resolution images have only been properly done in HL Tau (Carrasco-González et al. 2019) and TW Hya and HD 163296 (this work). The ages and characteristics of these disks are very different, for instance TW Hya is the oldest (∼10 Myrs) with a mass of 0.6 $M_\odot$ and a luminosity of 0.23 $L_\odot$, then goes HD 163296 (∼5 Myrs) with a mass and a luminosity of 1.9 $M_\odot$ and 17 $L_\odot$ respectively, and HL Tau is the youngest (∼1 Myr) with a mass and a luminosity somewhere in between the values of these two disks. HD 163296 and HL Tau are very rich in substructures at millimeter wavelengths showing several bright and dark rings with different contrasts and widths, while TW Hya shows much narrower and shallower substructures.

The results in both disks compared to HL Tau can give a hint of how the dust evolution is related to the formation of planetary systems. Our results indicate that in TW Hya and HD 163296 we have particle sizes > 1 millimeter at radii > 20 au and up to 100 au. Unfortunately we can't study the dust properties at radii < 20 au because the emission is optically thick at the studied wavelengths. In order to study the dust properties in this region, it will be necessary to observe at longer wavelengths, like 7 millimeters, but we can anticipate that larger (∼ 1 cm) particles should be found at the internal parts of these disks. The situation in HL Tau seems to be less evolved: the larger particles seem to be of millimeters sizes and they can only be found in the internal parts of the disk (< 40 au), in the outer dense rings particles are smaller than 1 millimeter. However, in TW Hya and HD 163296, which are both older than HL Tau (1 Myr), particles seem to have already grown up to millimeter sizes in the hole disk and we can expect to find larger particles in the internal parts of these disks. Therefore, the results obtained in these three disks could be an indication of dust growth.

In the three cases, the gaps are less dense and have smaller particles than the bright rings. However, there are some differences. In HL Tau and HD 163296 there is a large gap at the outer parts of the disks. This is interesting because deep gaps are expected in the presence of an accreting protoplanet (Zhu 2015). In contrast, in TW Hya gaps are narrower and they don't seem to be very deep. This suggests that HL Tau and HD 163296 have already formed planets, most likely giant gaseous planets, while TW Hya may have formed giant gaseous planets long ago or it may have only formed sub-Neptune planets.

In the three cases, bright rings seem to be associated with dense material containing larger particles. This dense rings are excellent places for the growth of dust to form planetesimals (e.g. Flock et al. 2015; Carrasco-González et al. 2016; Ruge et al. 2016; Sierra et al. 2017; Sierra et al. 2019; Macías et al. 2019). It is likely that our results point to this. Note that HL Tau and HD 163296 both have a dense ring accumulating particles at a large radius ($\sim$ 100 au) and in both cases these dense rings are adjacent to a large and deep gap. Then, it is expected that particles in these rings are not allowed to migrate to the inner radii, then the subsequent evolution of the dust can be considered detached from the rest of the disk. However, in HL Tau particles have grown to micron sizes while in HD 163296 they have grown up to 1 millimeter. This strongly support that rings are important for the growth of dust since HD 163296 (5 Myrs) is significantly older than HL Tau (1 Myr).

In the case of the young HL Tau disk it has been suggested that there is a difference in the origin of the substructures in the outer disk and the inner disk. As commented above, in the outer disk there is evidence for the presence of a giant planet. However, the internal ($<$ 40 au) structures seems to be related with the presence of snowlines (Carrasco-González et al. 2019). Note that the most important snowlines take place at temperatures $>$ 50 K (e.g. H_2O, NH_3, HCN, CO_2, CH_3OH; Zhang et al. 2015). Therefore, in the case of TW Hya all important snowlines are located approximately at 3 au and in the case of HD 163296 almost all snowlines are also in the inner part of the disk ($<$ 10 au). Only the CO2 snowline might be associated with the most internal gap of HD 163296. These results suggest that the effect of the presence of snowlines in the radial particle distribution is important for the formation of the substructures and the growth of dust only at very early stages when the disk is warmer. For disks older than 1 Myr substructures are most likely related to the presence of protoplanets. In the case of HD 163296 and HL Tau we see large and deep gaps which are most probably related to the presence of giant planets, this suggests that giant planets could be formed very early in the evolution of the disks. Interestingly TW Hya does not show a similar structure, but it does show narrower gaps which could be associated with the presence of rocky planets.

Note that the integrated dust mass is still higher for the large particles solution than most of the studies regarding the dust mass in protoplanetary disks (e.g. Bergin and Williams 2018). A possible explanation of this difference could be that these studies assume that there is no scattering and that the disks are completely optically thin. But, as we mention in the first chapter, these assumptions might not be correct and this might result in the underestimation of the total disk dust mass. Note that, it is possible that our simplification of the disk structure with height is still resulting in an underestimation of the disk dust mass (Tapia et al. 2019).

More solid conclusions should be based on a larger number of well studied disks. However, this kind of studies are very expensive in observational time and we should wait several years before we can have a representative sample. Moreover, a proper study needs observations at

longer wavelengths in order to study the most internal parts and the larger particles in disks (e.g. Carrasco-González et al. 2016; Carrasco-González et al. 2019), but this is even more expensive at this moment since the VLA is the only interferometer able to obtain high quality images at these wavelengths. We should wait for the construction of the next generation VLA to go further on this kind of analysis (Andrews et al. 2018b).

Note that all this discussion is only based on the results of three disks, however these are the three only cases that a detailed analysis of the dust particle distribution has been performed. Nevertheless, note that this picture fits very well with the time scale estimated for protoplanetary disks ($\sim$ 3 Myrs)(Ribas et al. 2015; Ansdell et al. 2016; Hernández et al. 2007). These studies suggest that giant gaseous planets should form very early ($\sim$ 1 Myr), while the formation of rocky planets could still take place a little later.

Bibliography

ALMA Partnership, Brogan, C. L., Pérez, L. M., et al. 2015, ApJ, 808, L3

Andrews, S. M., Wilner, D. J., Hughes, A. M., et al. 2012, ApJ, 744, 162

Andrews, S. M., Wilner, D. J., Zhu, Z., et al. 2016, ApJ, 820, L40

Andrews, S. M., Huang, J., Pérez, L. M., et al. 2018a, ApJ, 869, L41

Andrews, S. M., Wilner, D. J., Macías, E., Carrasco-González, C., & Isella, A. 2018b, Science with a Next Generation Very Large Array , 517, 137

Andrews, S. M. 2020, arXiv e-prints, arXiv:2001.05007

Ansdell, M., Williams, J. P., van der Marel, N., et al. 2016, ApJ, 828, 46

Bae, J., Zhu, Z., & Hartmann, L. 2017, ApJ, 850, 201

Barge, P., & Sommeria, J. 1995, A&A, 295, L1

Beckwith, S. V. W., Sargent, A. I., Chini, R. S., & Guesten, R. 1990, AJ, 99, 924

Bergin, E. A., Cleeves, L. I., Gorti, U., et al. 2013, Nature, 493, 644

Bergin, E. A. & Williams, J. P. 2018, arXiv e-prints, arXiv:1807.09631

Birnstiel, T., Dullemond, C. P., Zhu, Z., et al. 2018, ApJ, 869, L45

Brauer, F., Dullemond, C. P., & Henning, T. 2008, A&A, 480, 859

Carrasco-González, C., Henning, T., Chandler, C. J., et al. 2016, ApJ, 821, L16

Carrasco-González, C., Sierra, A., Flock, M., et al. 2019, ApJ, 883, 71

Chiang, E. I., & Goldreich, P. 1997, ApJ, 490, 368

Dong, R., Liu, S. Y., Eisner, J., et al. 2018, ApJ, 860, 124

Drazkowska, J., Li, S., Birnstiel, T., et al. 2019, ApJ, 885, 91

Dullemond, C. P., Birnstiel, T., Huang, J., et al. 2018, ApJ, 869, L46

D'Alessio, P., Calvet, N., & Hartmann, L. 2001, ApJ, 553, 321

Flock, M., Ruge, J. P., Dzyurkevich, N., et al. 2015, A&A, 574, A68

Gaia Collaboration, Brown, A. G. A., Vallenari, A., et al. 2016, A&A, 595, A2

Gaia Collaboration, Brown, A. G. A., Vallenari, A., et al. 2018, ArXiv e-prints.

Galván-Madrid R., Liu H. B., Izquierdo A. F., Miotello A., Zhao B., Carrasco-González C., Lizano S., Rodríguez L. F., 2018, ApJ, 868, 39

Gorti, U., Hollenbach, D., Najita, J., & Pascucci, I. 2011, ApJ, 735, 90

Guilloteau, S., Dutrey, A., Piétu, V., & Boehler, Y. 2011,A&A, 529, A105

Hernndez J., Calvet N., Briceo C., Hartmann L., Berlind P., 2004, AJ, 127, 1682

Hernández, J., Calvet, N., Briceño, C., et al. 2007, ApJ, 671, 1784

Huang, J., Andrews, S. M., Cleeves, L. I., et al. 2018, ApJ, 852, 122

Huang, J., Andrews, S. M., Dullemond, C. P., et al. 2018, ApJ, 869, L42

Isella, A., Testi, L., Natta, A., et al. 2007, A&A, 469, 213

Isella, A., Natta, A., Wilner, D., et al. 2010, ApJ, 725, 1735

Isella, A., Guidi, G., Testi, L., et al. 2016, Physical Review Letters, 117, 251101

Isella, A., Huang, J., Andrews, S. M., et al. 2018, ApJ, 869, L49

Ishimaru, A. 1978, Wave Propagation and Scattering in Random Media, Vol. 1 (New York: Academic)

Johansen, A., & Lambrechts, M. 2017, Annual Review of Earth and Planetary Sciences, 45, 359

Keppler, M., Benisty, M., Müller, A., et al. 2018, A&A, 617, A44

Liu, Y., Henning, T., Carrasco-González, C., et al. 2017, A&A, 607, A74

Liu, H. B. 2019, ApJ, 877, L22

Macías, E., Espaillat, C., Osorio, M., et al. 2019, ApJ(in press, arXiv:1907.07277)

Mathis, J. S., Rumpl, W., & Nordsieck, K. H. 1977, ApJ, 217, 425

Mendigutía, I., Brittain, S., Eiroa, C., et al. 2013, ApJ, 776, 44

Menu, J., van Boekel, R., Henning, T., et al. 2014, A&A, 564, A93

Miyake, K., & Nakagawa, Y. 1993, Icarus, 106, 20

Montesinos, B., Eiroa, C., Mora, A., & Merín, B. 2009, A&A, 495, 901

Muro-Arena, G. A., Dominik, C., Waters, L. B. F. M., et al. 2018, A&A, 614, A24

Muzerolle, J., Hillenbrand, L., Calvet, N., Hartmann, L., & Briceo, C. 2001, in Astronomical Society of the Pacific Conference Series, Vol. 244, Young Stars Near Earth: Progress and Prospects, ed. R. Jayawardhana & T. Greene, 245 Natta, A., Testi, L., Alcalá, J. M., et al. 2014, A&A, 569, A5

Nomura, H., Tsukagoshi, T., Kawabe, R., et al. 2016, ApJ, 819, L7

Okuzumi, S., Momose, M., Sirono, S., Kobayashi, H., & Tanaka, H. 2016, ApJ, 821, 82

Okuzumi, S., & Tazaki, R. 2019, ApJ, 878, 132

Pérez, L. M., Chandler, C. J., Isella, A., et al. 2015, ApJ, 813, 41

Pérez, L. M., Carpenter, J. M., Andrews, S. M., et al. 2016, Science, 353, 1519

Pinte, C., Dent, W. R. F., Ménard, F., et al. 2016, ApJ, 816, 25

Pinilla, P., Pohl, A., Stammler, S. M., & Birnstiel, T. 2017, ApJ, 845, 68

Pollack, J. B., Hollenbach, D., Beckwith, S., et al. 1994, ApJ, 421, 615

Qi, C., Ho, P. T. P., Wilner, D. J., et al. 2004, ApJ, 616, L11

Rau, U., & Cornwell, T. J. 2011, A&A, 532, 71

Ribas, Á., B. Merín, H. Bouy, et al., 2014, A&A, 561, A54

Ribas, A., Bouy, H., & Merín, B. 2015, A&A, 576, A52

Robitaille, T. P., Whitney, B. A., Indebetouw, R., & Wood, K. 2007, ApJS, 169, 328

Rodmann, J., Henning, T., Chandler, C. J., Mundy, L. G., & Wilner, D. J. 2006,A&A, 446, 211

Ruge, J. P., Flock, M., Wolf, S., et al. 2016, A&A, 590, A17

Sallum, S., Follette, K. B., Eisner, J. A., et al. 2015, Nature, 527, 342

Setterholm B. R., Monnier J. D., Davies C. L., et al. 2018, ApJ, 869, 164

Sierra, A., Lizano, S., & Barge, P. 2017, ApJ, 850, 115

Sierra, A., Lizano, S., Macías, E., et al. 2019, ApJ, 876, 7

Sierra, A. & Lizano, S. 2020, arXiv e-prints, arXiv:2003.02982

Sokal K. R., Deen C. P., Mace G. N., Lee J.-J., Oh H., Kim H., Kidder B. T., Jaffe D. T., 2018, ApJ, 853, 120

Tapia, C., Lizano, S., Sierra, A., Carrasco-González, C., & Bayona-Bobadilla, E. 2019, ApJ, 887, 244

Tazzari, M., Testi, L., Ercolano, B., et al. 2016, A&A, 588, A53

Testi, L., Birnstiel, T., Ricci, L., et al. 2014, Protostars and Planets VI (Tucson, AZ: University of Arizona Press), 339

Tilling, I., Woitke, P., Meeus, G., et al. 2012, A&A, 538, A20

Tsukagoshi, T., Nomura, H., Muto, T., et al. 2016, ApJ, 829, L35

Tsukagoshi, T., Muto, T., Nomura, H., et al. 2019, ApJ, 878, L8

van der Marel, N., Williams, J. P., Ansdell, M., et al. 2018b, ApJ, 854, 177

Whipple, F. L. 1972 in From Plasma to Planet, ed. A. Evlius (New York, NY: Wiley), 211

White, R. J., & Hillenbrand, L. A. 2004, ApJ, 616, 998

Williams, J. P., & Cieza, L. A. 2011, ARA&A, 49:1, 67

Wilner, D. J., D'Alessio, P., Calvet, N., Claussen, M. J., & Hartmann, L. 2005, ApJ, 626, L109

Zhang, K., Blake, G., & Bergin, E. 2015, IAU General Assembly, 22, 56118

Zhang, K., Bergin, E. A., Blake, G. A., et al. 2016, ApJ, 818, L16

Zhang, S., Zhu, Z., Huang, J., et al. 2018, ApJ, 869, L47

Zhu, Z. 2015, ApJ, 799, 16

Zhu, Z., Stone, J. M., Rafikov, R. R., et al. 2014, ApJ, 785, 122

Zhu, Z., Zhang, S., Jiang, Y.-F., et al. 2019, ApJ, 877, L18